Title: The structure of the human cell cycle

One-sentence summary: A systems-level view of single-cell states reveals the underlying architecture of the human cell cycle

Authors:

Wayne Stallaert[1,2], Katarzyna M. Kedziora[1,3], Colin D. Taylor[1,2], Tarek M. Zikry[2,4], Holly K. Sobon[1,2], Sovanny R. Taylor[1,2], Catherine L. Young[1,2], Juanita C. Limas[5], Jeanette G. Cook[5,6] and Jeremy E. Purvis[1,2,*]

Affiliations:

[1]Department of Genetics, University of North Carolina at Chapel Hill, Chapel Hill, NC, USA.

[2]Computational Medicine Program, University of North Carolina at Chapel Hill, Chapel Hill, NC, USA.

[3]Bioinformatics and Analytics Research Collaborative, University of North Carolina at Chapel Hill, Chapel Hill, NC, USA.

[4]Department of Biostatistics, Gillings School of Global Public Health, University of North Carolina, Chapel Hill, NC, USA.

[5]Department of Pharmacology, University of North Carolina at Chapel Hill, Chapel Hill, NC, USA.

[6]Department of Biochemistry and Biophysics, University of North Carolina at Chapel Hill, NC, USA.

***Corresponding Author:**

Jeremy Purvis

Mary Ellen Jones Building 11018C, CB#7488

116 Manning Drive

Chapel Hill, NC 27599-7488

jeremy_purvis@med.unc.edu

ABSTRACT:

The human cell cycle is conventionally depicted as a five-phase model consisting of four proliferative phases (G1, S, G2, M) and a single state of arrest (G0). However, recent studies show that individual cells can take different paths through the cell cycle and exit into distinct arrest states, thus necessitating an update to the canonical model. We combined time lapse microscopy, highly multiplexed single cell imaging and manifold learning to determine the underlying "structure" of the human cell cycle under multiple growth and arrest conditions. By visualizing the cell cycle as a complete biological process, we identified multiple points of divergence from the proliferative cell cycle into distinct states of arrest, revealing multiple mechanisms of cell cycle exit and re-entry and the molecular routes to senescence, endoreduplication and polyploidy. These findings enable the visualization and comparison of alternative cell cycles in development and disease.

Main text:

Our current understanding of the human cell cycle has been assembled piecemeal from decades of individual biochemical and genetic experiments (*1*). The earliest studies focused on the identification of discrete phases of DNA synthesis and cell division (*2*). Advances in molecular biology led to the identification of key cell cycle effectors (e.g. cyclins and cyclin-dependent kinases (CDKs)) and an understanding of the molecular events controlling the DNA replication, mitosis, and cell cycle arrest. This accumulated knowledge has resulted in the adoption of a model that separates the cell cycle into four functionally distinct proliferative phases (G1, S, G2 and M) and cell cycle arrest (G0). This five-phase cell cycle model, which has shaped our thinking for over 70 years (*3*), provides a useful framework for mapping key molecular events that govern the progression of a typical cell through the cell cycle.

However, a wave of recent single-cell studies in cultured cells has revealed that progression through the cell cycle cannot be reduced to a single, fixed sequence of molecular events. Cells can progress at different rates through each of the proliferative phases (*4*–*7*) and vary in the precise molecular paths taken through these phases (*8*–*11*). For example, some cells re-enter the cell cycle immediately following mitosis and begin the molecular preparations for DNA replication in S phase. Other cells divert temporarily to a reversible cell cycle arrest known as quiescence and re-enter the cell cycle after some variable amount of time. Under some conditions, cells can loop back to an earlier point in the cell cycle in response to certain stresses encountered during G1 (*9*, *10*) or divert to a different mechanistic route when the canonical path is blocked by pharmacological inhibition (*8*). These studies collectively imply that the cell cycle is a plastic process in which cells may traverse different mechanistic routes *en route* to DNA replication and cell division.

It has been especially difficult to study the behavior of cells once they have exited the proliferative cell cycle and entered a state of cell cycle arrest. It is known, for example, that after entering quiescence individual cells re-enter the cell cycle after variable lengths of time (*11*–*16*), but the mechanisms that regulate this decision remain unclear. It also appears that certain quiescent states can become “deeper” with time, requiring a larger or longer stimulus in order to reverse this arrest and resume the cell cycle (*17*–*19*). In

some cases, cells may become irreversibly arrested or "senescent" (*20*–*22*). Precisely how this state varies at the molecular level from reversible arrest has been a longstanding question for the field.

Recent work has begun using single cell measurements to describe the heterogeneity in cell cycle progression. For example, studies using single-cell mRNA sequencing have revealed considerable variability in the transcriptional states of individual cells around a single, cyclical cell cycle trajectory (*23*–*25*). One advantage of these methods is the ability to capture the expression of thousands of different transcripts in the same cell in an unbiased manner. However, models based on transcriptional measurements alone cannot capture many of the core mechanisms known to regulate cell cycle progression. It is widely appreciated that progression through the cell cycle is primarily driven by changes in protein turnover, post-translational modifications or the subcellular localization of key effectors (*1*) — features that cannot be captured by transcriptomics. Other studies using protein-based measurements to study cell cycle progression in individual cells have been focused on mapping the dynamics of cell cycle effectors along a single, one-dimensional trajectory through the proliferative cell cycle (*26*, *27*). These approaches are useful for understanding the temporal profile of cell cycle proteins but cannot detect the higher order relationships among effectors in individual cells (e.g., the relationships between cyclins, CDKs, and CDK inhibitors) that are necessary to understand the overall architecture of fate trajectories.

To look for evidence of heterogeneity in cell cycle progression and to better understand the mechanistic basis of this plasticity, we performed time lapse imaging to record the individual cell cycle histories of human epithelial cells followed by iterative immunofluorescence of 48 core cell cycle regulators to obtain high-dimensional, protein-based cell cycle signatures of >30,000 individual cells. We used manifold learning to project these cells onto two- and three-dimensional surfaces to visualize the cell cycle as a sequence of continuous molecular states, ultimately revealing the underlying "structure" of the cell cycle. We also mapped the architecture of cell cycle arrest using various cell cycle stresses, identifying multiple points of divergence from the proliferative cell cycle into distinct states of arrest with unique molecular signatures. In addition, we revealed the fate trajectory through which sustained replication stress can generate polyploidy

following mitotic skipping and a general mechanism through which cells can overcome p21 induction and re-enter the cell cycle by increasing the expression of proliferative effectors such as cyclin D.

Probing the structure of the cell cycle

Starting with an asynchronous population of non-transformed human retinal pigmented epithelial cells (hTERT-RPE-1, abbreviated hereafter as RPE cells, **Fig. 1A**) expressing a single fluorophore cell cycle reporter (PCNA-mTurquoise2 (mTq2)) (*28*), we performed time lapse imaging to record the cell cycle histories of individual cells, including the cell cycle phase (i.e. G0/G1, S, G2 or M) and age (i.e. time elapsed since previous mitosis) of each cell (**Fig. 1B)**. Following time lapse imaging, cells were fixed and then subjected to multiple rounds of immunofluorescence using iterative indirect immunofluorescence imaging (4i) to obtain measurements of 48 core cell cycle effectors (**Table S1**) in a total of 8850 individual cells. From this imaging dataset we extracted 246 single-cell features including the expression and localization of each protein (i.e. in the nucleus, cytosol, perinuclear region and plasma membrane), cell morphological features (e.g. the size and shape of the nucleus and cell), and features of the microenvironment (e.g. local cell density), culminating in a multivariate cell cycle signature for each cell in the entire population.

We then used machine learning to (1) enrich our feature set for variables that best predict the cell cycle state of each cell and (2) eliminate features that vary among cells in a cell cycle-independent manner (see Methods). To do so, we used ground truth annotations of cell cycle phase and age obtained by time lapse imaging to train random forest classifiers to predict these measures of cell cycle 'state' solely from the 4i signatures of individual cells (with a 95.5% accuracy for phase and an RMSE=125.8 min and R^2=0.862 for age predictions). We then averaged the rank order of feature importance from the phase and age models to obtain a combined ranking for each feature. Successive random forests were generated for both phase and age by increasing the number of training features in order of this combined ranking to determine the minimal feature set necessary to accurately predict cell cycle state (i.e. both phase and age) and minimize redundancies (**fig. S1A-C, Table S2**).

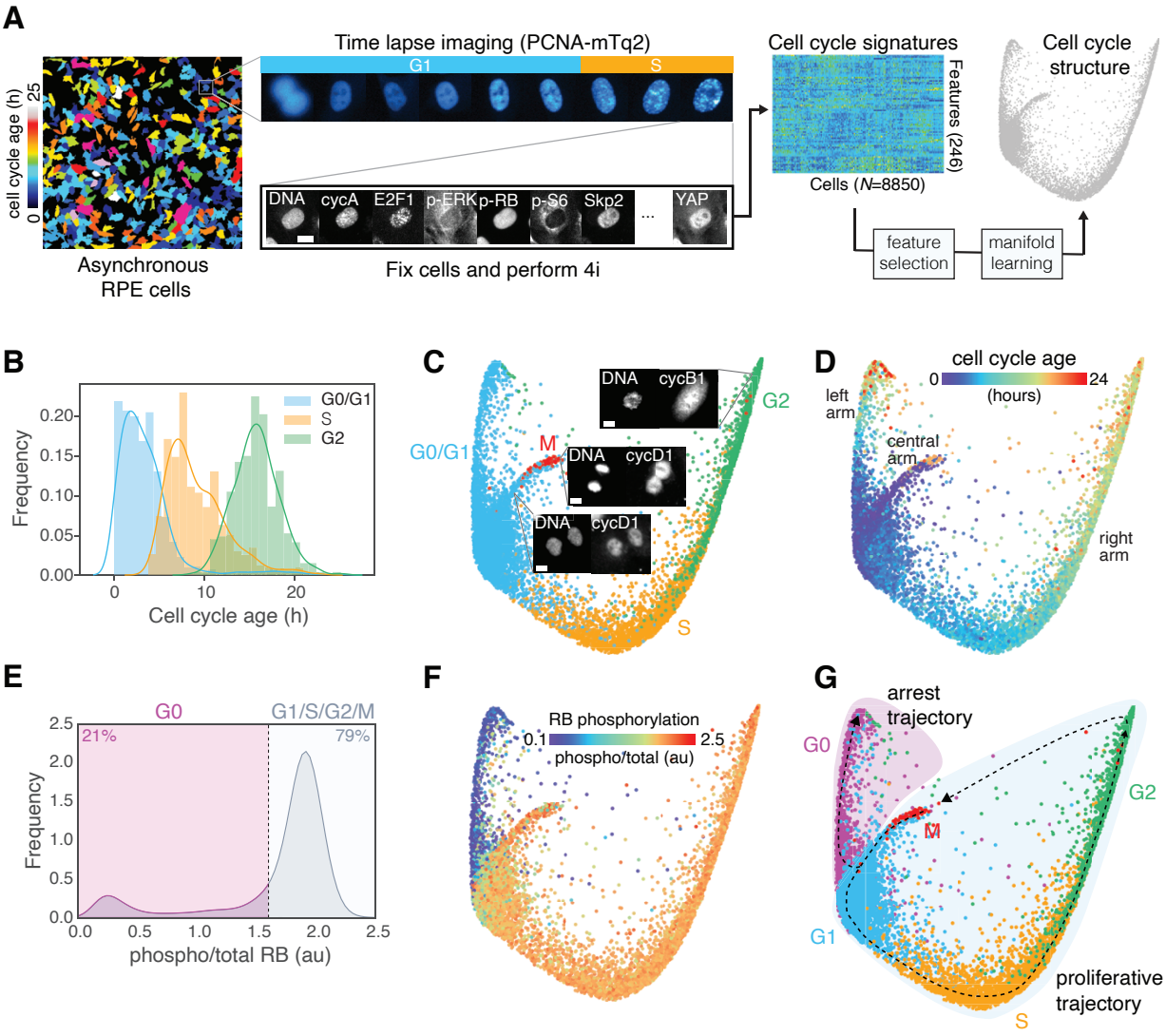

Figure 1. Probing the structure of the cell cycle. (**A**) Schematic of the experimental approach. (**B**) Distributions of cell cycle phase and age (time since mitosis) of all cells annotated by time-lapse imaging. (**C-D**) Cell cycle phase (C) and age (D) annotations/predictions (see Methods) of 8850 individual cells mapped onto the cell cycle structure. Representative images of mitotic cells and their locations on the structure are shown in (C). (**E-F**) Distribution of RB phosphorylation (phospho/total nuclear intensity) in individual cells (E) and mapped on the structure (F). (**G**) Proliferative (G1/S/G2/M) and arrest (G0) trajectories through the five canonical phases. Scale bars = 10 μm.

We reasoned that cells at similar positions in the cell cycle should possess similar cell cycle signatures (as defined by 4i), and thus be located close to one another on a lower dimensional manifold within the high-dimensional space of this minimal feature set. To identify and visualize this manifold, we used Potential of Heat-diffusion for Affinity-based Transition Embedding (PHATE), a nonlinear manifold learning approach that performs well for continuous and branched trajectories in high-dimensional space (*29*).

This data-driven approach produced a continuous, three-armed structure representing the collective cell cycle states of every cell in the population (2D structure in **Fig. 1**; 3D structure in **Movies 1-4**; virtual reality-compatible dataset available (see Acknowledgments)). We found that this three-armed structure was reproducible across PHATE parameter space (**fig. S2A**), individual replicates (**fig. S2B**) and in another human epithelial cell line (human pancreatic epithelial cells, HPNE, **fig. S2C**).

Cell cycle annotations were obtained by time lapse imaging for only a subset of cells (33%) in order to preserve a temporal resolution that can accurately delineate cell cycle phase transitions (1 frame/16 min) (**fig. S1D-E**, see Methods). We used the random forest models that were trained to predict cell cycle phase and age based on the 4i signatures of cells (described above) to infer the cell cycle phase and age of cells that were not captured by time lapse imaging (**Fig. 1C-D, Movies S2** and **S3**). Similar inferences were obtained using a convolutional neural network trained on the same data (Phase: 95.7% accuracy, concordance with RF model = 94.8%; Age: RMSE = 123.7 min; **fig. S1F-K**). Mapping the cell cycle phase of each cell onto the structure, we observed that G0/G1 cells encompass most of the left and central arms, while S and G2 cells progressively reside along the rightmost arm, respectively (**Fig. 1C**). While cell cycle progression towards mitosis is clearly represented along the right arm of the structure, M phase cells were located at the tip of the central arm. Visual inspection of the immunofluorescence images of cells along the central arm revealed a progression through nuclear envelope reformation and cytokinesis, events consistent with the late stages of mitosis. Similarly, cells at the tip of the right arm possessed features of late G2 and early M, including DNA condensation and nuclear envelope breakdown. Mapping cell cycle age onto the structure indicated that the youngest cells lie near the tip of the central arm where newborn cells emerge out of mitosis and into G1, and that age increases as cells progress up both the left and right

arms (**Fig. 1D**). The close correspondence between cell cycle age (determined by time lapse imaging) and the continuum of molecular states in the structure (determined by the similarity of 4i cell cycle signatures) provided confirmation that this structure represents an accurate depiction of the temporal trajectories of the cell cycle.

While the PCNA-mTq2 reporter allows delineation of the proliferative phases of the cell cycle (G1/S/G2/M) (*28*), it cannot distinguish G0 from G1 cells. The phosphorylation and inactivation of the retinoblastoma protein (RB), on the other hand, represents a major checkpoint controlling cell cycle re-entry and is often used to define the boundary between G0 (i.e. cell cycle arrest) and G1 (i.e. cell cycle commitment) (*30*–*32*). In our 4i data, we observed bimodality in RB phosphorylation (**Fig. 1E**), and a clear delineation between these two cellular states (high vs. low RB phosphorylation) along the central arm, thus distinguishing G0 from G1 cells (**Fig. 1F, Movie 4**). We use this RB phosphorylation status to identify actively proliferating versus arrested cells throughout the manuscript.

We therefore infer two principal trajectories within this cell cycle structure: (1) a cyclical, *proliferative trajectory* starting at the base of the central arm and progressing along the right arm through G1, S and G2, before looping back to the central arm during mitosis, and (2) an *arrest trajectory* along the left arm (**Fig. 1G**).

Mapping the mechanisms of the proliferative cell cycle (G1/S/G2/M)

To validate our approach, we used cell cycle age annotations to order cells temporally along the proliferative trajectory and examined key mechanisms previously shown to drive cell cycle progression (**Auxiliary fig. S1**). This approach successfully ordered key molecular events regulating the G1/S transition (**Fig. 2A**) (*33*). The core molecular unit regulating this decision is the RB-mediated inhibition of E2F transcription factors, which control the expression of various S phase genes (*34*). Commitment to DNA replication is triggered by the phosphorylation and inhibition of RB by cyclin:CDK complexes. In early G1, RB is primarily phosphorylated by cyclin D:CDK4/6 (*16*), and we observed that cells begin their cell cycle with high cyclin D1 expression (**Fig. 2B**). This cyclin D:CDK4/6-driven phosphorylation of RB in early G1 de-represses E2F-

regulated genes important for DNA replication including expression of E2F1 itself (**Fig 2C**) (*35*, *36*). E2F activity also stimulates the production of cyclin E (**Fig. 2D**), which activates CDK2 to maintain RB phosphorylation as cyclin D levels begin to decrease (**Fig. 2B**) (*16*, *27*). Another important event in the G1/S transition is the inactivation of APC/C complexes, which degrade and prevent the accumulation of S phase proteins during G1. The increase in cyclin E:CDK2 activity in late G1 stimulates the destruction of the Cdh1 subunit (**Fig. 2E**), switching off APC/C and permitting S phase initiation (*9*). The inactivation of APC/C also allows cyclin A to accumulate as S phase begins (**Fig. 2F**) to replace cyclin E and maintain CDK2-dependent RB phosphorylation through to mitosis (**Fig. 2D**).

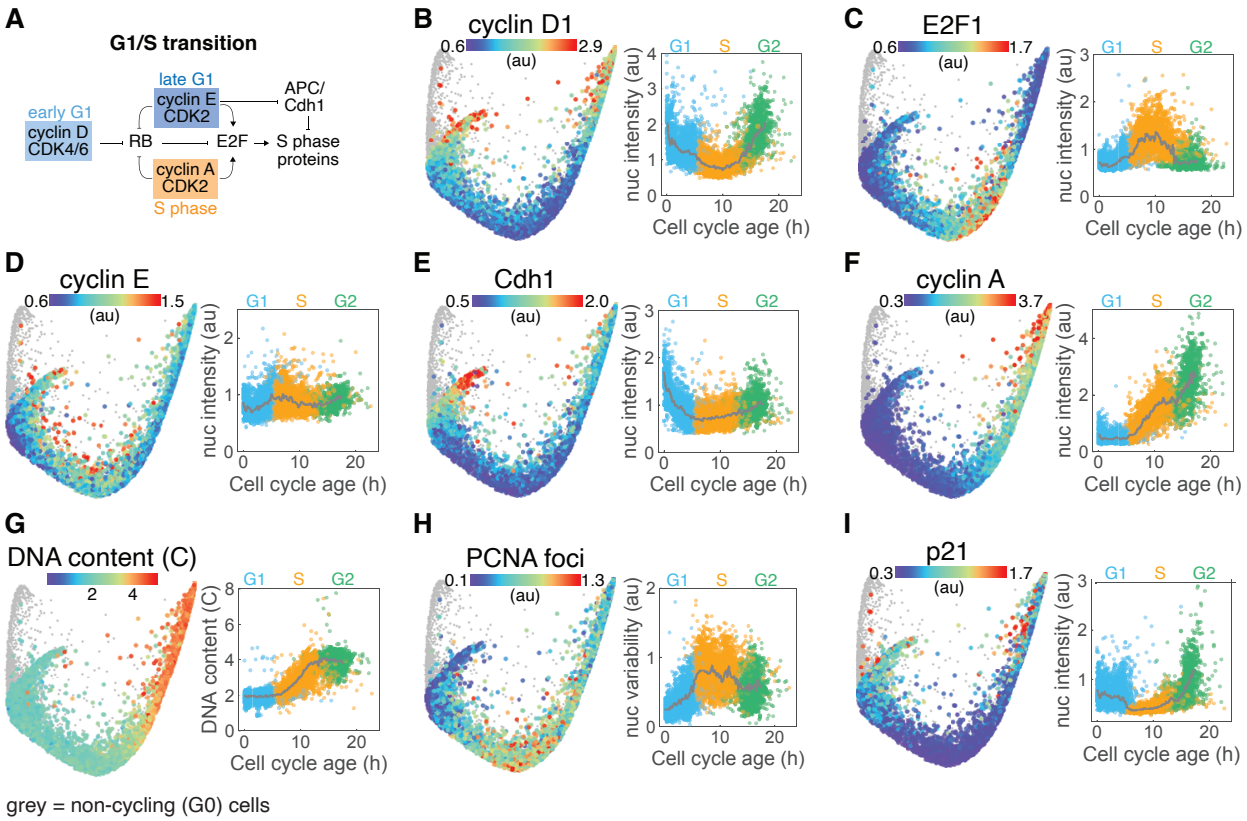

Figure 2. Visualizing the mechanisms of the G1/S transition. (**A**) Mechanistic model of the core events regulating progress through G1 and the transition to S. (**B-I**) Median nuclear intensity of cyclin D1 (B), E2F1 (C), cyclin E (D), Cdh1 (E), cyclin A (F) and p21 (I), DNA content (copy number) (G), and variability in nuclear PCNA intensity (H) of cells in the proliferative trajectory are mapped onto the cell cycle structure (left panels) and plotted against cell cycle age (right panels). Population medians in time courses indicated by solid grey lines and individual cells are colored by cell cycle phase (G1: blue, S: orange, G2: green). Non-cycling (G0) cells (phospho/total RB < 1.6) are shown in grey on the structure and are excluded from time courses.

DNA replication was clearly visible on the structure, with DNA content doubling over the course of S phase (**Fig. 2G**). Similarly, we localized additional S phase events important for DNA replication including the appearance of PCNA foci at replication complexes (quantified as variability in nuclear intensity) (**Fig. 2H**) and the replication-coupled destruction of p21 (**Fig. 2I**). Upon entry into G2, cyclin B expression increases first in the cytoplasm and then in the nucleus (**fig. S3A-B**) as cells move toward mitosis (*37*). We also observed increases in cyclin D1 (**Fig. 2B**) and its transcription factor cMyc (**fig. S3C**) as well as NF-kB activation (**fig. S3D**) during G2, which then remained elevated through mitosis and into the subsequent G1 phase of daughter cells, resulting in U-shape dynamics along the proliferative trajectory (*27*). Taken together, this approach accurately recapitulated many of the key molecular events governing the progression of cells through the four proliferative cell cycle phases.

Trajectories into and out of cell cycle arrest (G0)

We used the same approach to examine the molecular changes that occur as cells progress along the arrest trajectory (**Auxiliary fig. S2**), for which comparatively less is known. We noted that cells exited mitosis with high RB phosphorylation along a single path down the central arm and then quickly diverged along two distinct trajectories within the first 2-3 hours following mitosis: either progressing directly into G1 with sustained RB phosphorylation or exiting the cell cycle into G0 following the loss of RB phosphorylation (**Fig. 3A, Fig. 1F, fig. S4A**). In each daughter cell, this fate decision was found to be governed primarily by the balance between cyclin D and p21 expression. Cyclin D and p21 activate and inhibit CDK4/6 activity, respectively, to control the phosphorylation state of RB in a stoichiometric and ultrasensitive manner (**fig. S4A-D**) (*13*, *14*, *38*). We found that the decrease in the cyclin D1:p21 ratio that precedes cell cycle exit was not due to a decrease in cyclin D1 expression, but rather an increase in p21 expression in early G1 (**Fig. 3B, fig. S4A**), consistent with previous observations (*38*). This induction of p21 in early G1 occurred simultaneously with the loss of RB phosphorylation as cells diverted to the arrest trajectory (**fig. S4A**).

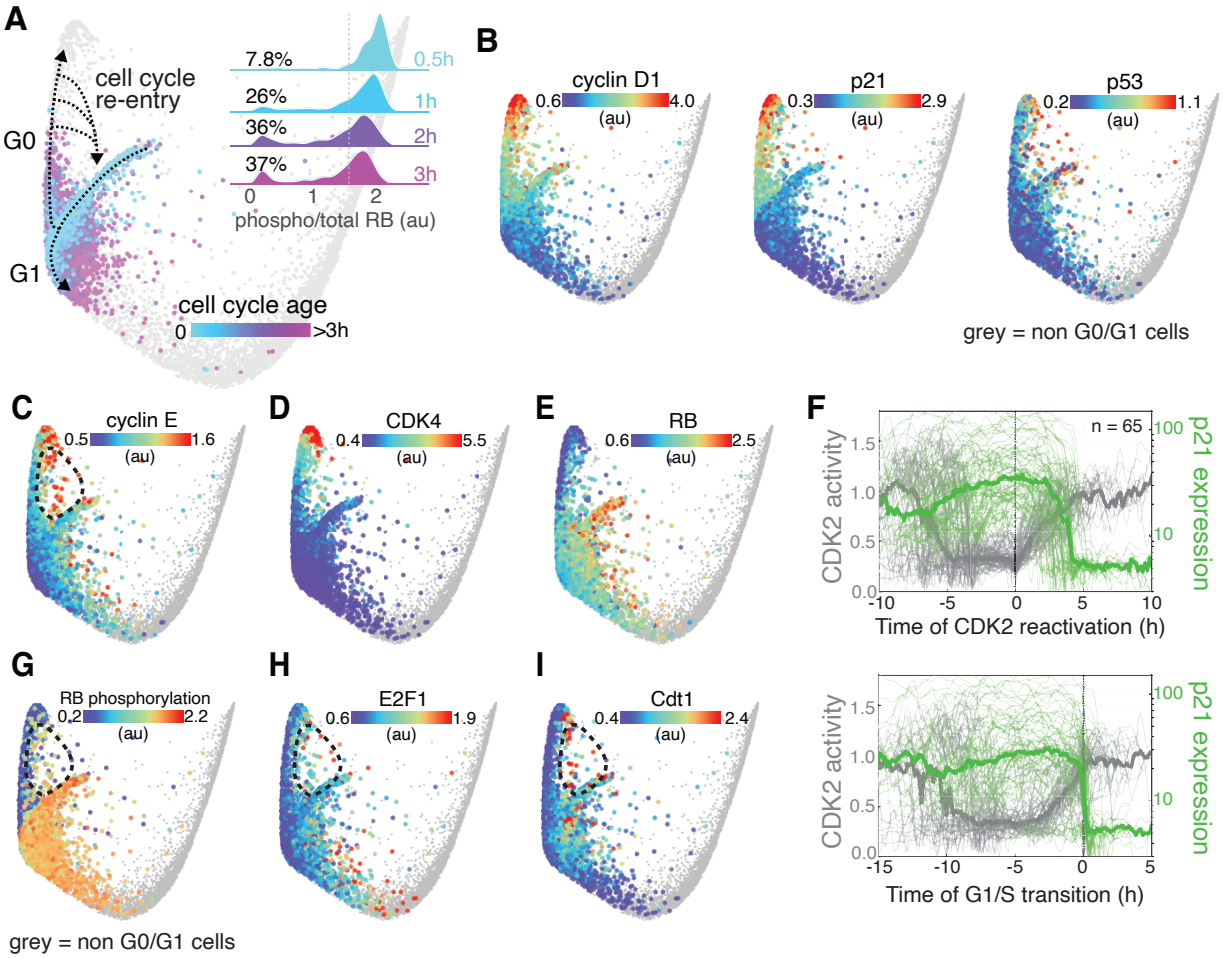

Figure 3. Cell cycle exit and re-entry from spontaneous arrest (G0). (**A**) Divergence of cell cycle trajectories into G1 or G0 following mitosis and subsequent cell cycle re-entry from G0. Cell cycle age of newborn cells (< 3h since mitosis) is mapped onto the structure. *Inset:* Time course of RB phosphorylation in individual cells following mitosis. Cells were binned by cell cycle age (less than 0.5, 1, 2 and 3 h post-mitosis). (**B**) Median nuclear expression of cyclin D1 (left), p21 (middle) and p53 (right) mapped onto G0/G1 cells. (**C-E**) Median nuclear expression of cyclin E (C), CDK4 (D) and RB (E) mapped onto G0/G1 cells. (**F**) Single cell traces from time-lapse imaging of CDK2 activity (grey, quantified by the cytoplasm:nuclear ratio of DHB-mCherry) and p21-YPet expression (green) aligned at the time of CDK2 reactivation (upper panel) and the G1/S transition (lower panel). Thick lines represent population medians. *N* = 65 cells. (**G-I**) RB phosphorylation (G) and median nuclear expression of E2F1 (H) and Cdt1 (I) mapped onto G0/G1 cells. Note the dotted circle representing cell cycle re-entry in C, G, H and I.

Further examination of the arrest trajectory revealed that cells do not exit the cell cycle into a single, static arrest state awaiting cell cycle re-entry. Instead, cells progressed further along this trajectory with time (**Fig. 1D**) accompanied by a progressive change in molecular signature suggesting an increasing depth of arrest (*18*, *19*, *22*, *27*). Cells with longer durations of arrest exhibited increases in the expression of p21, p53 (**Fig. 3B**), p38 and p16 (**fig. S5**). Surprisingly, progression further up the arrest arm was also accompanied by increases in cyclin D1 (**Fig. 3B**), cyclin E, and CDK4 expression, along with loss of RB expression (**Fig. 3C-E**), molecular changes that typically promote cell cycle progression, not arrest.

We therefore hypothesized that cells may re-enter the cell cycle not by reversing the increase in p21 expression that drove cell cycle exit but instead by overcoming it with excessive cyclin and/or CDK expression. To test this hypothesis, we performed time lapse imaging of RPE cells engineered using a CRISPR-Cas9 knock-in approach to express fluorescently-tagged endogenous p21 (p21-YPet), a marker of cell cycle phase (PCNA-mTq2) and a CDK2 activity sensor (DHB-mCherry) to monitor cell cycle exit and re-entry (*12*). We observed that the re-activation of CDK2 as cells emerged from arrest occurred prior to a reduction in p21 (**Fig. 3F**). Instead, a decrease in p21 expression was observed only later, as cells transitioned into S phase due to its replication-coupled destruction (**Fig. 3F**) (*15*). Furthermore, the majority of cells (83%) re-entered the cell cycle (as identified by the reactivation of CDK2) at equal or higher p21 expression than was required to inhibit CDK2 activation during cell cycle exit immediately after cell division (**fig. S4E**), indicating that a reduction in p21 expression to baseline is not a prerequisite for cell cycle re-entry and that the CDK activity required to progress through G1 and into S phase can be achieved instead by mechanisms that overcome elevated p21 expression.

Cells re-enter the cell cycle along a funnel-shaped trajectory on the inside of the structure, connecting various points along the arrest arm with the base of the central arm (**Fig. 3A**). Cells in this region showed increased expression of cyclin D1 (**Fig. 3B**), a high cyclin D1:p21 ratio (**fig. S4C**) and high RB phosphorylation (**Fig. 3G, Movie S4**), consistent with cell cycle re-entry. Having spent variable amounts of time in G0, these cells are relatively old compared to other G1 cells (**Fig. 1D, Movie S2**), and exhibit characteristics of cells preparing for DNA replication including increased expression of cyclin E (**Fig. 3C**),

E2F1 (**Fig. 3H**) and Cdt1 (**Fig. 3I**). Cell cycle re-entry therefore is not simply a reversal of the mechanisms that drive cells into arrest, but instead occurs along a distinct molecular trajectory back to the proliferative cell cycle.

Cellular senescence

In addition to changes in their molecular state, cells also increased in size as they progressed further along the arrest trajectory with time (**fig. S6A, Fig. 1D**), a phenomenon first observed in yeast cell cycle arrest (*39*). In particular, cells residing at the end of the arrest trajectory (**Fig. 4A**) were at least 3-4 times larger than the average arrested cell and possessed a high cytoplasm-to-DNA ratio (**Fig. 4B**), a hallmark of cellular senescence (*40*). Cells in this terminal arrest region also showed the longest durations of arrest (>18 h, **Fig. 1D**) and exhibited a unique molecular signature that was distinct from other cells in the arrest arm. This molecular profile included increased expression of DNA damage markers phospho-H2AX, phospho-CHK1, p38 (**fig. S6B-D**) and p53 (**Fig. 4C**), CDK inhibitors p21, p27 and p16 (**fig. S6E-G**), and loss of the proliferative effectors PCNA and Fra1 (**fig. S6H-I**). These cells also exhibited a cytoplasmic dilution of CDK2 (**Fig. 4D**) and increased nuclear expression of β-catenin (**Fig. 4E**), an effector known to mediate signaling during senescence induction (*41*). Cells located in this region possessed either 2 or 4 copies of DNA (2C or 4C, **Fig. 4F**) (and no multinucleated cells were observed), indicating that some cells must have exited the proliferative cell cycle along a second arrest trajectory that diverts after DNA replication (**Fig. 4A**). Indeed, we identified a population of cells residing

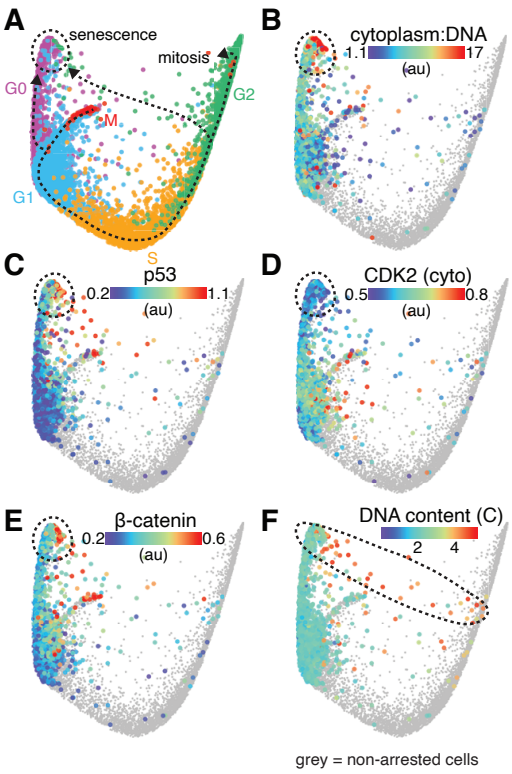

Figure 4. Signature of cellular senescence. (**A**) Model showing two distinct molecular trajectories into senescence, diverging from the proliferative cell cycle in either G1 or G2. (**B-F**) Ratio of cytoplasmic area:DNA content (B), median nuclear expression of p53 (C) and β-catenin (E), median cytoplasmic expression of CDK2 (D) and DNA content (copy number) (F) of arrested cells are mapped onto the structure. Non-arrested cells (phospho/total RB > 1.6) are shown in grey.

along a path between G2 and the arrest terminus with 4 copies of DNA (**Fig. 4F, Movie S1**), elevated markers of a DNA damage response (**Fig. 4C**, **fig. S6B-E**) and a loss of RB phosphorylation (**Fig. 1F**).

The molecular architecture of cell cycle arrest

To further explore the architecture of cell cycle arrest, we performed 4i and manifold learning on >23,000 cells following treatment with a variety of stresses known to induce cell cycle arrest: hypomitogenic stress induced by serum starvation, replication stress following etoposide treatment and oxidative stress in response to hydrogen peroxide (**Fig. 5**). Plotting the arrest trajectories in response to each of these stresses on the same map alongside unperturbed cells provided a clear visualization of the complex architecture of cell cycle arrest and its connectivity with the proliferative cell cycle (**Fig. 5A**).

In response to hypomitogenic stress (i.e. serum starvation for 1 or 7 days), cells diverged from the proliferative cell cycle in G2, undergoing cell division directly into a state of arrest with 2C DNA content ("$G0_{hypomitogenic}$", **Fig. 5A**) identified by the loss of RB phosphorylation (**Fig. 5B**). However, unlike the spontaneous arrest observed in unperturbed cells (**Fig. 3B**), exit to the hypomitogenic arrest state was accompanied by only a modest increase in p21, and instead was driven primarily by a loss of cyclin D1 expression (**Fig. 5B, fig. S7**). Following serum starvation, cells do not exhibit the characteristic increase in cyclin D1 during G2 that is observed in the cell cycle of unperturbed cells (**Fig. 5B, Fig. 2B**). Consequently, RB phosphorylation is rapidly lost due to a lack of cyclinD1:CDK4/6 activity (*16*) as cells complete mitosis. Progression further along this trajectory was accompanied by an increase in p27 (**Fig. 5B**) and loss of CDK4 and CDK6 (**fig. S8**), consistent with previous observations that hypomitogenic arrest is not a single static state but rather a continuum of states of deeper quiescence (*18*, *19*, *22*). The hypomitogenic arrest state was also characterized by decreased expression of key proliferative effectors Cdh1, Cdt1, Fra1 and cJun, as well as decreased nuclear YAP and mTOR signaling (S6 phosphorylation) (**Fig. 5C, fig. S8**).

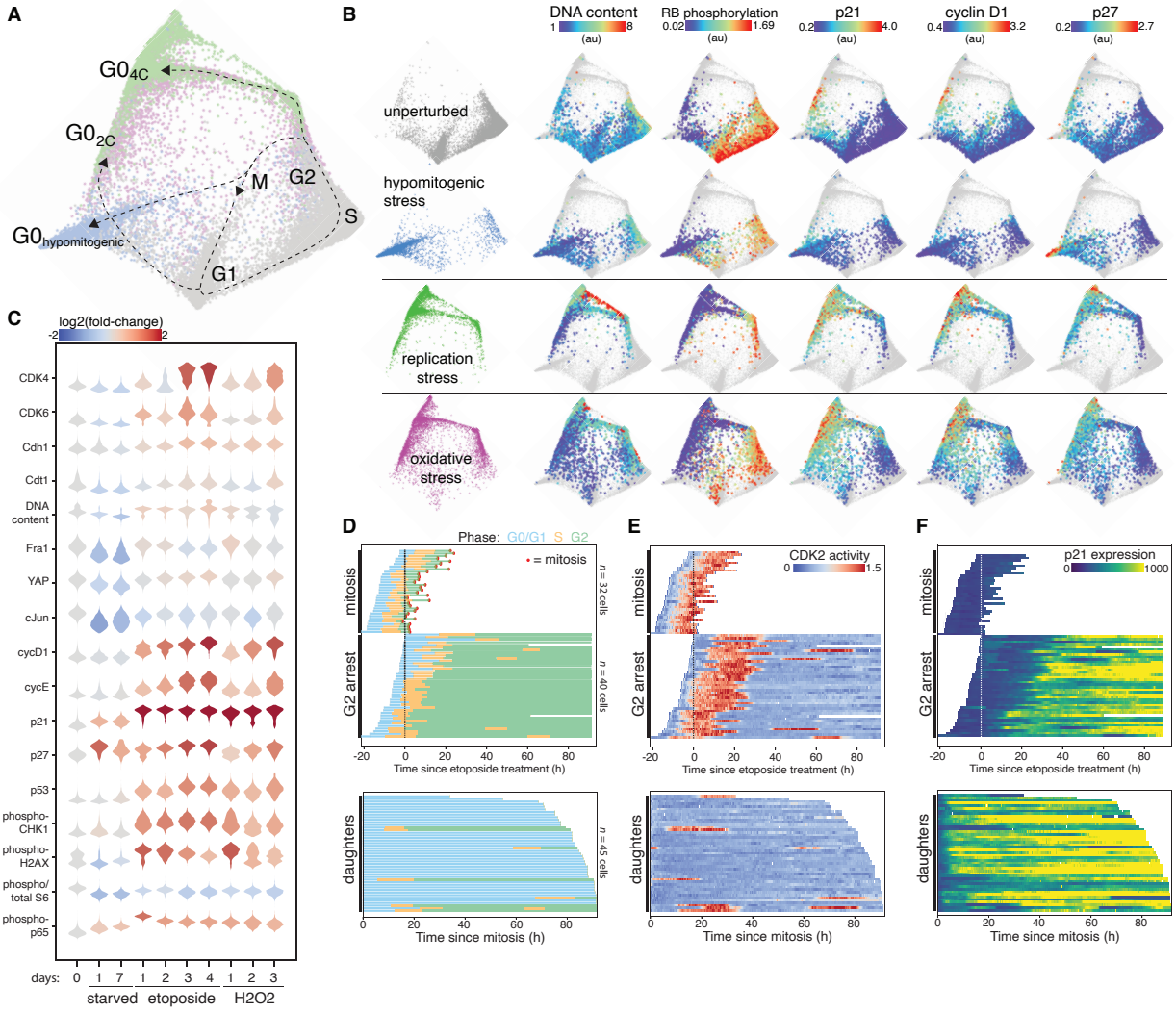

Figure 5. The architecture of cell cycle arrest. (**A**) Expanded cell cycle structure depicting the proliferative phases (G1/S/G2/M) and multiple states of arrest (G0). Unperturbed (grey, *N* = 11,268 cells), serum-starved ("hypomitogenic stress", 1 or 7 days, blue, *N* = 3007 cells), etoposide-treated ("replication stress", 1 µM for 1-4 days, green, *N* = 4315 cells) and H2O2-treated ("oxidative stress", 200 µM for 1-3 days, purple, *N* = 5015 cells) cells are mapped onto the structure. (**B**) DNA content, RB phosphorylation and median nuclear expression of p21, cyclin D1 and p27 are mapped onto unperturbed and stressed cells. For panels A and B, all time points for each treatment are mapped on the structure. (**C**) Molecular signatures of cell cycle stresses over time. Single cell distributions are colored by relative expression versus control. (**D-F**) Single cell tracks derived from time lapse imaging depicting cell cycle phase (D, manually annotated based on presence of PCNA foci in S phase), CDK2 activity (E, quantified by the cytoplasm:nuclear ratio of DHB-mCherry) and p21-YPet expression (F, median nuclear intensity) following 1 µM etoposide treatment. G2 arrested and mitotic fates (upper panels) and daughters of mitotic cells (lower panels) are shown. *N* = 117 cells.

We next assessed how the cell cycle responds to replication stress following treatment with etoposide (for 1, 2, 3 or 4 days), an inhibitor of DNA topoisomerase II that interferes with DNA re-ligation during replication. Within a single population of cells treated with etoposide, we observed that individual cells exited the proliferative cell cycle along two distinct arrest trajectories: (1) from a G2-like state after DNA replication was complete (DNA content = 4C), or (2) in the subsequent G1 phase of daughter cells immediately following mitosis (DNA content = 2C) (**Fig. 5A**). Cell cycle exit to the 4C state ("$G0_{4C}$") was accompanied by the activation of the DNA damage checkpoint in G2, including an increase in DNA damage itself (pH2AX), activation of CHK1, NF-κB signaling (phospho-p65) and increased expression of p53 (**fig. S9**) and p21 (**Fig. 5B, fig. S7**), while daughter cells that exit to the 2C state following mitosis ("$G0_{2C}$") possessed elevated p21 expression but showed no increase in other DNA damage markers (**Fig. 5B, fig. S9**). While a few unperturbed cells were found to populate both the hypomitogenic and 4C states of arrest, the majority of spontaneously arrested cells (with low RB phosphorylation) were observed along a trajectory towards the 2C arrest state driven by an increase in p21 but exhibiting very weak expression of DNA damage markers (**Fig. 5B, fig. S9**), consistent with observations that spontaneous cell cycle arrest results from low levels of replication stress (*38*).

To validate the observation that individual cells may exit the cell cycle along two distinct arrest trajectories in response to replication stress and to investigate the mechanisms that govern this fate decision, we performed single cell time lapse imaging of RPE cells expressing a cell cycle sensor (PCNA-mTq2), a CDK2 activity sensor to detect cell cycle arrest (DHB-mCherry) (*12*) and endogenous p21 fused to a fluorophore (p21-YPet) for ~4 days after etoposide treatment (**Fig 5D-F, fig. S10**). We observed a similar bifurcation of cell fate in live cells in response to replication stress, with 56% of cells arresting in G2 and 44% proceeding through to mitosis following etoposide treatment (**Fig. 5D, upper panel**). For each of these cells that successfully completed mitosis, however, we observed that their daughter cells arrested immediately following cell division (as indicated by a sustained decrease in CDK2 activity) (**Fig. 5D, lower panel**). Choice between these two fate trajectories was dependent on the timing of p21 induction in individual cells. While G2 arrest coincided with a loss of CDK2 activity and an increase in p21 expression soon after the S/G2 transition (**Fig. 5E-F, upper panel; fig. S10A**), in cells that proceeded through to mitosis, p21

remained low in G2 (**Fig. 5F, upper panel; fig. S10B**) but increased abruptly following cell division in daughter cells (**Fig. 5F, lower panel; fig. S10C**). Furthermore, daughter cell cycle arrest was found to be reversible, with some cells re-entering the cell cycle and transitioning into S phase after variable lengths of time in G0 (**Fig. 5D, bottom panel**). These cells, however, invariably arrested as they transitioned into G2, due to the persistent stress of etoposide during DNA replication, consistent with the observation that cells progressively escaped from the 2C arrest state and accumulated in the 4C state over time following etoposide treatment (**Fig. 6A-B**).

To assess the cell cycle response to oxidative stress, we treated cells with hydrogen peroxide (H_2O_2) for 1, 2 or 3 days. We observed very similar arrest architecture to replication stress (**Fig. 5A-B**), indicating that the dominant cell cycle response to exogenous oxidative stress is primarily related to its known ability to induce DNA damage (**Fig. 5B-C, fig. S9**)(*42*). Similar to etoposide treatment, H_2O_2 induced cell cycle exit along two distinct trajectories diverging from either G1 or G2, into arrest states with 2C or 4C DNA content, respectively, both accompanied by p21 induction (**Fig. 5B, fig. S7**). However, unlike etoposide, H_2O_2 is rapidly metabolized following addition to cells (*43*) and consequently induces only temporary stress soon after treatment. Consistent with a transient DNA damage response, markers of DNA damage decrease more rapidly (**Fig 5C, fig. S11A-B**) and a higher proportion of cells remain in the cell cycle over time (**fig. S11C-D**).

Mitosis skipping and polyploidization

While the 2C state of cell cycle arrest following etoposide-induced replication stress was found to be reversible (**Fig. 5D-E, bottom panels**), the accumulation of cells in the 4C state over time (**Fig. 6A-B**) suggested that it may represent an irreversible state of cell cycle arrest. As cells progressed along the arrest trajectory from G2 to the 4C arrest state (**Fig. 6A, pink arrow**), there was an abrupt degradation of the S/G2 cyclins A and B (**Fig. 6C-D**) that coincided with the loss of RB phosphorylation (**Fig. 5B**). Degradation of these cyclins normally occurs during mitosis (*44*). However, we observed no change in DNA content (**Fig. 6B**) nor any visual evidence of mitotic events in the images of cells along this trajectory. Progression further along this trajectory was accompanied by an increase in G1 cyclins D1 and E, as well

as an increase in Cdh1 and a loss of Skp2 (**Fig. 6E-H**), all consistent with the transition into a G0/G1-like state and a phenomenon known as “mitotic skipping”, which often precedes the transition into senescence (*45*–*47*). Indeed, after 3 days of etoposide treatment, most cells resided in a G0/G1-like state of cell cycle arrest with 4C DNA content (**Fig. 6B**) and a high cytoplasm-to-DNA ratio (**Fig. 6I**), consistent with a senescent state (*40*, *47*).

However, following a trajectory upward from the 4C arrest state (**Fig. 6A,** *purple arrow*), we observed molecular changes consistent with cell cycle re-entry and progress toward S phase, including sequential increases in cyclin D1, cyclin E and the DNA licensing factor Cdt1 (**Fig. 6E,F,J**). Furthermore, there was a gradual accumulation of polyploid cells with 8C DNA content over time following etoposide treatment (**Fig. 6B**), supporting a hypothesis that cells might be able to re-enter the cell cycle from this 4C state of arrest and undergo a second round of DNA replication, or “endoreduplication” (*48*), without prior cell division. To validate these observations, we performed time lapse imaging for 4 days following etoposide treatment. We observed rare instances of cells re-entering the cell cycle from the 4C state of arrest (as indicated by an increase in CDK2 activity) and transitioning into a second S phase (as indicated by an increase in PCNA foci) without undergoing mitosis (5/117 cells over 4 days of imaging; **Fig. 6K, Fig. 5D**). Similar to cell cycle re-entry in unperturbed cells (**Fig. 3**), the re-emergence of cells from the 4C state of arrest following mitotic skipping occurred despite elevated p21 expression (**Fig. 5B,6K**) in cells with very high expression of cyclin D1 (**Fig. 6E**). To test if increased cyclin D expression can overcome p21 expression and drive endoreduplication, we treated cells with siRNA against all three cyclin D isoforms following etoposide treatment. Knockdown of cyclin D completely abolished the appearance of polyploid cells in response to replication stress (**Fig. 6L**), confirming its role in the generation of polyploidy, and indicating that increased expression of G1 cyclins may represent a general mechanism through which cells can escape p21-induced cell cycle arrest.

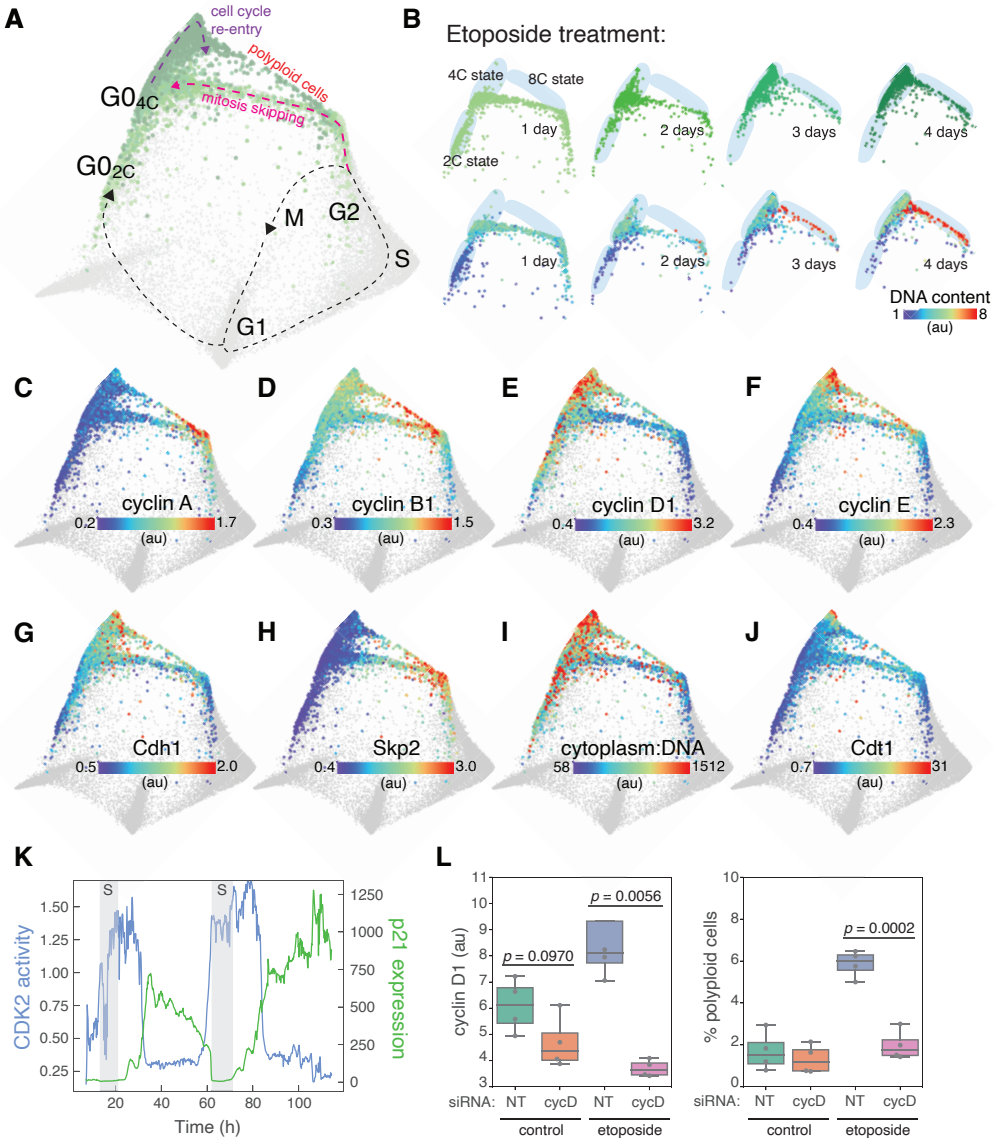

Figure 6. Mitosis skipping and polyploidization. (**A**) Cell fate trajectories in response to replication stress. Unperturbed (grey) and etoposide-treated (1 μM, green) cells are mapped onto the structure. (**B**) Changes in the proportion of cells with 2C, 4C and 8C DNA content over time following etoposide treatment. (**C-J**) Median nuclear intensities of cyclin A (C), cyclin B1 (D), cyclin D1 (E), cyclin E (F), Cdh1 (G), Skp2 (H) and Cdt1 (J) and the cytoplasm:DNA ratio (I) of etoposide-treated cells are mapped onto the expanded cell cycle structure. Data from all time points (1-4 days) are plotted together on each structure. (**K**) Representative single cell trace showing mitotic skipping and endoreduplication observed during time lapse imaging. Two S phases were identified by the appearance of PCNA nuclear foci and are depicted by grey bars. CDK2 activity (quantified by the cytoplasm:nuclear ratio of DHB-mCherry, blue) and p21-YPet expression (green) are shown. (**L**) Cyclin D1 expression (left) and the proportion of polyploid cells (right) measured by Hoechst staining and immunofluorescence, respectively, following siRNA-mediated knockdown of cyclin D in control and etoposide pre-treated cells. Bars represent population medians from four independent replicates (grey circles) and statistical significance was determined using a two-tailed Student's *t* test.

Discussion

We combined time lapse microscopy, multiplexed imaging, and manifold learning to reveal the underlying structure of the human epithelial cell cycle. This data-driven approach revealed the molecular architecture of proliferative and arrested states as well as a detailed map of the connectivity between them.

Under standard cell culture conditions, we observed a single proliferative trajectory through DNA replication and cell division. The primary source of heterogeneity observed among unperturbed cells occurred shortly after cell division, when the molecular trajectories of newborn daughter cells diverged along two distinct paths, either immediately re-entering the cell cycle or diverting into a spontaneous arrest state driven by an induction of p21 expression (**Fig. 3**), as previously described (*12*, *14*, *32*, *49*). Although an alternative mechanistic route through G1 has recently been observed when the canonical route is blocked (i.e. by CDK4/6 inhibition)(*8*), our results indicate that, when grown under ideal culture conditions, cells primarily traverse a single trajectory *en route* to mitosis. This topology was reproducibly obtained from replicate cell populations, across PHATE parameter space and in a second human epithelial cell line (**fig. S2**).

We mapped the architecture of cell cycle arrest states using various cell cycle stresses, revealing multiple molecular trajectories diverging from different points in the proliferative cell cycle into distinct arrest states (**Fig. 5**). In response to mitogen starvation, for example, cells followed a graded trajectory into a single arrest state characterized by a lack of cyclin D and an increase in p27. In contrast, replication or oxidative stress caused cells to exit the proliferative cell cycle along two distinct arrest trajectories: diverting either in G2 or immediately after cell division. The choice between these divergent arrest trajectories was determined by distinct p21 dynamics in response to DNA damage.

In addition, we found that increased expression of proliferative effectors such as cyclin D1, cyclin E and CDK4/6 was a general feature of all arrest states driven by p21 induction, promoting cell cycle re-entry from the spontaneous arrest observed in control cells (**Fig. 3**), the 2C arrest state following replication and oxidative stress (**Fig. 4**) and from the 4C arrest state that follows mitotic skipping, which in this particular case leads to endoreduplication and polyploidization (**Fig. 6**). As a general principle, these findings indicate

that cell cycle re-entry does not necessarily require a reversal of the mechanisms that induced arrest, but can occur instead along a distinct molecular trajectory, in some cases by overcoming sustained arrest signals with countervailing proliferative signals.

The systems-level approach described in the current study allows many of the core regulatory events governing cell cycle progression and arrest to be quantified and visualized simultaneously on a single representation and using a single assay. Here, we demonstrated how this approach can identify how the cell cycle responds to different stresses. This comparative cell cycle analysis may prove particularly powerful in the context of cancer cell biology. Identifying differences between normal and oncogenic cell cycle structures may provide novel insights into the mechanisms of tumorigenesis and lead to the development of new therapeutic targets.

Acknowledgments:

We would like to thank Sonja Mihailovic (UNC Chapel Hill), Chi Pham (UNC Chapel Hill) and Margaret Redick (Oregon State University) for assistance with cell culture and Dr. Sam Wolff (UNC Chapel Hill) for support with imaging. We would like to thank Dr. Robert Duronio (UNC Chapel Hill) and Dr. Adam Palmer (UNC Chapel Hill) for careful reading of the manuscript. **Funding:** This work was supported by grants from R01-GM138834 (JEP), DP2-HD091800 (JEP), and NSF CAREER Award 1845796 (JEP). **Authors contributions:** WS and JEP conceived of the project. WS, KMK, JGC and JEP designed the experiments. WS, HKS, SRT and CLY performed the 4i experiments. WS and SRT performed the time lapse imaging. WS, KMK and CDT performed image analysis. TMZ trained the random forest models. KMK trained the neural networks. HKS and CLY performed Western blots. JCL created the RPE-dox-KRAS cell line. WS wrote the manuscript with the help of all authors. **Competing interests:** The authors declare no competing interests. **Data and materials availability:** Single cell datasets, including data compatible for exploration in virtual reality, are available at http://doi.org/10.5281/zenodo.4525425.

Supplementary Materials

Materials and Methods

Table S1 - S2

Fig S1 - S12

Auxiliary Figures S1 - S2

Movies S1 - S4

References

1. D. O. Morgan, *The Cell Cycle: Principles of Control* (New Science Press, 2007).

2. A. Howard, S. R. Pelc, Nuclear incorporation of P32 as demonstrated by autoradiographs. *Exp. Cell Res.* **2**, 178–187 (1951).

3. A. Howard, S. R. Pelc, Synthesis of nucleoprotein in bean root cells. *Nature*. **167**, 599–600 (1951).

4. J. A. Smith, L. Martin, Do cells cycle? *Proc. Natl. Acad. Sci. U. S. A.* **70**, 1263–1267 (1973).

5. R. Shields, Transition probability and the origin of variation in the cell cycle. *Nature*. **267**, 704–707 (1977).

6. A. R. Araujo, L. Gelens, R. S. Sheriff, S. D. Santos, Positive Feedback Keeps Duration of Mitosis Temporally Insulated from Upstream Cell-Cycle Events. *Mol. Cell*. **64**, 362–375 (2016).

7. H. X. Chao, R. I. Fakhreddin, H. K. Shimerov, K. M. Kedziora, R. J. Kumar, J. Perez, J. C. Limas, G. D. Grant, J. G. Cook, G. P. Gupta, J. E. Purvis, Evidence that the human cell cycle is a series of uncoupled, memoryless phases. *Mol. Syst. Biol.* **15**, e8604 (2019).

8. C. Liu, Y. Konagaya, M. Chung, L. H. Daigh, Y. Fan, H. W. Yang, K. Terai, M. Matsuda, T. Meyer, Altered G1 signaling order and commitment point in cells proliferating without CDK4/6 activity. *Nat. Commun.* **11**, 5305 (2020).

9. S. D. Cappell, M. Chung, A. Jaimovich, S. L. Spencer, T. Meyer, Irreversible APC Cdh1 Inactivation Underlies the Point of No Return for Cell-Cycle Entry. *Cell*. **166**, 167–180 (2016).

10. S. D. Cappell, K. G. Mark, D. Garbett, L. R. Pack, M. Rape, T. Meyer, Emi1 switches from being a substrate to an inhibitor of APC/CCdh1 to start the cell cycle. *Nature*. **558**, 313 (2018).

11. H. W. Yang, S. D. Cappell, A. Jaimovich, C. Liu, M. Chung, L. H. Daigh, L. R. Pack, Y. Fan, S. Regot, M. Covert, T. Meyer, Stress-mediated exit to quiescence restricted by increasing persistence in CDK4/6 activation. *Elife*. **9** (2020), doi:10.7554/eLife.44571.

12. S. L. Spencer, S. D. Cappell, F. C. Tsai, K. W. Overton, C. L. Wang, T. Meyer, The proliferation-quiescence decision is controlled by a bifurcation in CDK2 activity at mitotic exit. *Cell*. **155**, 369–383 (2013).

13. K. W. Overton, S. L. Spencer, W. L. Noderer, T. Meyer, C. L. Wang, Basal p21

controls population heterogeneity in cycling and quiescent cell cycle states. *Proc. Natl. Acad. Sci. U. S. A.* **111**, E4386–93 (2014).

14. H. W. Yang, M. Chung, T. Kudo, T. Meyer, Competing memories of mitogen and p53 signalling control cell-cycle entry. *Nature*. **549**, 404–408 (2017).

15. A. R. Barr, S. Cooper, F. S. Heldt, F. Butera, H. Stoy, J. Mansfeld, B. Novak, C. Bakal, DNA damage during S-phase mediates the proliferation-quiescence decision in the subsequent G1 via p21 expression. *Nat. Commun.* **8**, 14728 (2017).

16. M. Chung, C. Liu, H. W. Yang, M. S. Köberlin, S. D. Cappell, T. Meyer, Transient Hysteresis in CDK4/6 Activity Underlies Passage of the Restriction Point in G1. *Mol. Cell*. **76**, 562–573.e4 (2019).

17. T. A. Owen, D. R. Soprano, K. J. Soprano, Analysis of the growth factor requirements for stimulation of WI-38 cells after extended periods of density-dependent growth arrest. *J. Cell. Physiol.* **139**, 424–431 (1989).

18. X. Wang, K. Fujimaki, G. C. Mitchell, J. S. Kwon, K. Della Croce, C. Langsdorf, H. H. Zhang, G. Yao, Exit from quiescence displays a memory of cell growth and division. *Nat. Commun.* **8** (2017), doi:10.1038/s41467-017-00367-0.

19. J. S. Kwon, N. J. Everetts, X. Wang, W. Wang, K. Della Croce, J. Xing, G. Yao, Controlling Depth of Cellular Quiescence by an Rb-E2F Network Switch. *Cell Rep.* **20**, 3223–3235 (2017).

20. P. Sousa-Victor, S. Gutarra, L. García-Prat, J. Rodriguez-Ubreva, L. Ortet, V. Ruiz-Bonilla, M. Jardí, E. Ballestar, S. González, A. L. Serrano, E. Perdiguero, P. Muñoz-Cánoves, Geriatric muscle stem cells switch reversible quiescence into senescence. *Nature*. **506**, 316–321 (2014).

21. S. Marthandan, S. Priebe, P. Hemmerich, K. Klement, S. Diekmann, Long-term quiescent fibroblast cells transit into senescence. *PLoS One*. **9**, e115597 (2014).

22. K. Fujimaki, R. Li, H. Chen, K. Della Croce, H. H. Zhang, J. Xing, F. Bai, G. Yao, Graded regulation of cellular quiescence depth between proliferation and senescence by a lysosomal dimmer switch. *Proc. Natl. Acad. Sci. U. S. A.* **116**, 22624–22634 (2019).

23. M. S. Kowalczyk, I. Tirosh, D. Heckl, T. N. Rao, A. Dixit, B. J. Haas, R. K. Schneider, A. J. Wagers, B. L. Ebert, A. Regev, Single-cell RNA-seq reveals changes in cell cycle and differentiation programs upon aging of hematopoietic stem cells. *Genome Res.* **25**, 1860–1872 (2015).

24. D. Schwabe, S. Formichetti, J. P. Junker, M. Falcke, N. Rajewsky, The transcriptome dynamics of single cells during the cell cycle. *Mol. Syst. Biol.* **16**, e9946 (2020).

25. M. Moussa, I. I. Măndoiu, Computational cell cycle analysis of single cell RNA-Seq data. *bioRxiv* (2020), p. 2020.11.21.392613.

26. G. Gut, M. D. Tadmor, D. Pe'er, L. Pelkmans, P. Liberali, Trajectories of cell-cycle progression from fixed cell populations. *Nat. Methods*. **12**, 951–954 (2015).

27. S. Gookin, M. Min, H. Phadke, M. Chung, J. Moser, I. Miller, D. Carter, S. L. Spencer, A map of protein dynamics during cell-cycle progression and cell-cycle exit. *PLoS Biol.* **15**, e2003268 (2017).

28. T. Zerjatke, I. A. Gak, D. Kirova, M. Fuhrmann, K. Daniel, M. Gonciarz, D. Müller, I. Glauche, J. Mansfeld, Quantitative Cell Cycle Analysis Based on an Endogenous All-in-One Reporter for Cell Tracking and Classification. *Cell Rep.* **19**, 1953–1966 (2017).

29. K. R. Moon, D. van Dijk, Z. Wang, S. Gigante, D. B. Burkhardt, W. S. Chen, K. Yim, A. van den Elzen, M. J. Hirn, R. R. Coifman, N. B. Ivanova, G. Wolf, S. Krishnaswamy, Visualizing structure and transitions in high-dimensional biological data. *Nat. Biotechnol.* **37**, 1482–1492 (2019).

30. A. B. Pardee, A restriction point for control of normal animal cell proliferation. *Proc. Natl. Acad. Sci. U. S. A.* **71**, 1286–1290 (1974).

31. A. Zetterberg, O. Larsson, Kinetic analysis of regulatory events in G1 leading to proliferation or quiescence of Swiss 3T3 cells. *Proc. Natl. Acad. Sci. U. S. A.* **82**, 5365–5369 (1985).

32. J. Moser, I. Miller, D. Carter, S. L. Spencer, Control of the Restriction Point by Rb and p21. *Proc. Natl. Acad. Sci. U. S. A.* **115**, E8219–E8227 (2018).

33. S. Hume, G. L. Dianov, K. Ramadan, A unified model for the G1/S cell cycle transition. *Nucleic Acids Res.* **48**, 12483–12501 (2020).

34. J. DeGregori, T. Kowalik, J. R. Nevins, Cellular targets for activation by the E2F1 transcription factor include DNA synthesis- and G1/S-regulatory genes. *Mol. Cell. Biol.* **15**, 4215–4224 (1995).

35. A. M. Narasimha, M. Kaulich, G. S. Shapiro, Y. J. Choi, P. Sicinski, S. F. Dowdy, Cyclin D activates the Rb tumor suppressor by mono-phosphorylation. *Elife*. **3** (2014), doi:10.7554/eLife.02872.

36. I. Sanidas, R. Morris, K. A. Fella, P. H. Rumde, M. Boukhali, E. C. Tai, D. T. Ting, M. S. Lawrence, W. Haas, N. J. Dyson, A Code of Mono-phosphorylation Modulates the Function of RB. *Mol. Cell*. **73**, 985–1000.e6 (2019).

37. S. D. M. Santos, R. Wollman, T. Meyer, J. E. Ferrell, Spatial Positive Feedback at the Onset of Mitosis. *Cell*. **149**, 1500–1513.

38. M. Arora, J. Moser, H. Phadke, A. A. Basha, S. L. Spencer, Endogenous Replication Stress in Mother Cells Leads to Quiescence of Daughter Cells. *Cell Rep.* **19**, 1351–1364 (2017).

39. G. C. Johnston, J. R. Pringle, L. H. Hartwell, Coordination of growth with cell division in the yeast Saccharomyces cerevisiae. *Exp. Cell Res.* **105**, 79–98 (1977).

40. G. E. Neurohr, R. L. Terry, J. Lengefeld, M. Bonney, G. P. Brittingham, F. Moretto, T. P. Miettinen, L. P. Vaites, L. M. Soares, J. A. Paulo, J. W. Harper, S. Buratowski, S. Manalis, F. J. van Werven, L. J. Holt, A. Amon, Excessive Cell Growth Causes Cytoplasm Dilution And Contributes to Senescence. *Cell*. **176**, 1083–1097.e18 (2019).

41. D.-Y. Zhang, H.-J. Wang, Y.-Z. Tan, Wnt/β-catenin signaling induces the aging of mesenchymal stem cells through the DNA damage response and the p53/p21 pathway. *PLoS One*. **6**, e21397 (2011).

42. B. Demple, J. Halbrook, Inducible repair of oxidative DNA damage in Escherichia coli. *Nature*. **304**, 466–468 (1983).

43. M. C. Sobotta, A. G. Barata, U. Schmidt, S. Mueller, G. Millonig, T. P. Dick, Exposing cells to H2O2: a quantitative comparison between continuous low-dose and one-time high-dose treatments. *Free Radic. Biol. Med.* **60**, 325–335 (2013).

44. M. Glotzer, A. W. Murray, M. W. Kirschner, Cyclin is degraded by the ubiquitin pathway. *Nature*. **349**, 132–138 (1991).

45. A. Sakaue-Sawano, T. Kobayashi, K. Ohtawa, A. Miyawaki, Drug-induced cell cycle modulation leading to cell-cycle arrest, nuclear mis-segregation, or endoreplication. *BMC Cell Biol.* **12**, 2 (2011).

46. M. Suzuki, M. Yamauchi, Y. Oka, K. Suzuki, S. Yamashita, Live-cell imaging visualizes frequent mitotic skipping during senescence-like growth arrest in mammary carcinoma cells exposed to ionizing radiation. *Int. J. Radiat. Oncol. Biol. Phys.* **83**, e241–50 (2012).

47. Y. Johmura, M. Shimada, T. Misaki, A. Naiki-Ito, H. Miyoshi, N. Motoyama, N. Ohtani, E. Hara, M. Nakamura, A. Morita, S. Takahashi, M. Nakanishi, Necessary and sufficient role for a mitosis skip in senescence induction. *Mol. Cell*. **55**, 73–84 (2014).

48. D. T. Fox, R. J. Duronio, Endoreplication and polyploidy: insights into development and disease. *Development*. **140**, 3–12 (2013).

49. M. Min, S. L. Spencer, Spontaneously slow-cycling subpopulations of human cells originate from activation of stress-response pathways. *PLoS Biol.* **17**, e3000178 (2019).

50. J. P. Matson, A. M. House, G. D. Grant, H. Wu, J. Perez, J. G. Cook, Intrinsic checkpoint deficiency during cell cycle re-entry from quiescence. *J. Cell Biol.* **218**, 2169–2184 (2019).

51. J.-Y. Tinevez, N. Perry, J. Schindelin, G. M. Hoopes, G. D. Reynolds, E. Laplantine, S. Y. Bednarek, S. L. Shorte, K. W. Eliceiri, TrackMate: An open and extensible platform for single-particle tracking. *Methods*. **115**, 80–90 (2017).

52. P. Thévenaz, U. E. Ruttimann, M. Unser, A pyramid approach to subpixel registration based on intensity. *IEEE Trans. Image Process.* **7**, 27–41 (1998).

53. F. A. Wolf, P. Angerer, F. J. Theis, SCANPY: large-scale single-cell gene expression data analysis. *Genome Biol.* **19**, 15 (2018).

54. D. F. Stein, H. Chen, M. E. Vinyard, L. Pinello, singlecellVR: interactive visualization of single-cell data in virtual reality. *Cold Spring Harbor Laboratory* (2020), p. 2020.07.30.229534.

Materials and Methods

Cell culture

Retinal pigment epithelial cells (hTERT RPE-1, ATCC, CRL-4000) were cultured in DMEM (Gibco, 11995-065) supplemented with 10% fetal bovine serum (FBS; Sigma, TMS-013-B), 2 mM L-glutamine (ThermoFisher Scientific, 25030081) and penicillin/streptomycin (P/S; ThermoFisher Scientific, 15140148). For time lapse imaging of RPE cells, FluoroBrite™ DMEM (Gibco, A18967-01) supplemented with 10% FBS and 2 mM L-glutamine was used. and Human pancreatic epithelial cells (hTERT-HPNE, ATCC, CRL-4023) were cultured in pyruvate-free DMEM (Gibco, 11965-092) supplemented with 10% FBS and P/S. All cells were cultured at 37 ºC and 5% CO_2.

Cell line generation

The construction of the RPE-PCNA-mTurqoise2 (RPE-mTq2) cell line was previously described (*7*). The RPE-PCNA-mTq2/p21-YPet/DHB-mCherry cell line was engineered using a CRISPR-Cas9 knock-in approach to introduce the YPet fluorophore into the 3' region of the endogenous p21 gene in a RPE-PCNA-mTq2/DHB-mCherry cell line (*50*). We synthesized the gene sequence for YPet-P2A-neoR (**fig. S12**) flanked by 900-950 bp homology arms into a pUC donor plasmid (Bio Basic Inc.) and targeted it to the endogenous p21 gene with the gRNA sequence ggaagccctaatccgcccac (Synthego). Recombinant Cas9 2.0 (Thermo Fisher Scientific, A36498) was mixed with gRNA and incubated for 15 min at room temperature. A total of $3x10^5$ cells were electroporated with 900 ng sgRNA and 3000 ng linearized donor plasmid using the Neon Transfection System (ThermoFisher Scientific). Positive clones were enriched using a low-dose of G418 (200 µg/ml), and individual clones were hand-picked and screened for successful fluorophore integration following overnight neocarzinostatin treatment to induce p21-YPet expression. The RPE-dox-KRAS cell line used in the cell stress 4i experiment was constructed by introducing the pInducer20 plasmid containing KRAS-G12V cDNA into RPE cells by viral transduction as described above. All cell lines were authenticated by STR profiling (ATCC) and confirmed to be mycoplasma free.

Antibodies

High quality, previously published/validated primary antibodies were identified using BenchSci (http://app.benchsci.com) and are listed in Table S1.

Time lapse imaging

Cells were plated in glass-bottom plates (Cellvis) coated with fibronectin (1 µg/cm^2, Sigma, F1141). Fluorescence images were acquired using a Nikon Ti Eclipse inverted microscope with a Nikon Plan Apochromat Lambda 40x objective with a numerical aperture of 0.95 and an Andor Zyla 4.2 sCMOS detector. Autofocus was provided by the Nikon Perfect Focus System (PFS) and a custom enclosure (Okolabs) was used to maintain constant temperature (37°C) and atmosphere (5% CO_2). For time lapse imaging, the following filter sets were used (excitation; beam splitter; emission filter; Chroma): CFP (425-445/455/465-495nm), YFP (490-510/515/520-550nm) and mCherry(540-580/585/593-668). Stitched 4-by-4 images were acquired every 10 min for RPE-PCNA-mTq2/p21-YPet/DHB-mCherry cells and every 16 min for RPE-PCNA-mTq2 cells. Uneven

field illumination was corrected prior to stitching. NIS-Elements AR software was used for image acquisition and post-processing. CDK2 activation was quantified as the ratio of background corrected cytoplasmic to nuclear intensity of the DHB-mCherry sensor (cytoplasm signal quantified as a 40th percentile in a 15-pixel ring outside the nuclear segmentation, with a 2-pixel gap between the nucleus and the ring; nuclear signal quantified as median) and p21-YPet expression was calculated as the background corrected median nuclear intensity. Cell cycle phases were annotated manually from time lapse imaging using the appearance/disappearance of nuclear PCNA foci to mark the beginning and end of S phase, respectively.

For the time lapse imaging that preceded 4i (**see Fig. 1A**), approximately 25% of the total well area was imaged for a total of 24h, permitting ~27% of the total cells to be tracked. Nuclear regions were segmented based on the PCNA-mTq2 signal using a modified U-Net neural network (https://github.com/fastai/fastai). Linking of regions into tracks was computed using TrackMate (*51*). Segmentation and tracking corrections were performed manually.

Iterative indirect immunofluorescence imaging (4i)

Cells were plated in glass-bottom plates (Cellvis) coated with fibronectin (1 μg/cm^2, Sigma, F1141), treated as required and prepared as follows. In between each step, samples were rinsed 3X times with phosphate-buffered saline (PBS) and incubations were at room temperature, unless otherwise stated. Cells were fixed with 4% paraformaldehyde (ThermoFisher Scientific, 28908) for 30 min, permeabilized with 0.1% Triton X-100 in PBS for 15 min and inspected for sample quality control following Hoechst staining in imaging buffer (IB: 700 mM N-acetyl-cysteine (Sigma, A7250) in ddH_2O. Adjust to pH 7.4). Sample was rinsed 3X with ddH_2O and incubated with elution buffer (EB: 0.5M L-Glycine (Sigma, 50046), 3M Urea (Sigma, U4883), 3M Guanidine chloride (ThermoFisher Scientific, 15502-016), and 70mM TCEP-HCl (Sigma, 646547) in ddH_20. Adjusted to pH 2.5) 3X for 10 min on shaker to remove Hoechst stain. Sample was incubated with 4i blocking solution (sBS: 100 mM maleimide (Sigma, 129585), 100 mM NH_4Cl (Sigma, A9434) AND 1% bovine serum albumin in PBS) for 1h and incubated with primary antibodies diluted as required (**Table S1**) in conventional blocking solution (cBS: 1% bovine serum albumin in PBS) overnight at 4°C. Samples were rinsed 3X with PBS and then incubated in secondary antibodies (**Table S1**) and Hoechst for 1h on shaker, then rinsed 5X with PBS and imaged in IB. Samples were imaged using the Nikon Ti Eclipse microscope described above. Stitched 8x8 images were acquired for each condition using the following filter cubes (Chroma): DAPI(383-408/425/435-485nm), GFP(450-490/495/500-550nm), Cy3(530-560/570/573-648nm), Cy5(590-650/660/663-738nm). After imaging, samples were rinsed 3X with ddH2O, antibodies were eluted and re-stained iteratively as described above.

Image processing and single cell analysis

Image registration was performed using a custom Python script (v3.7.1) using features common to multiple rounds (Hoechst or CDK2 staining) and StackReg library (*52*). Segmentation and feature extraction from registered images were performed using standard modules in CellProfiler (v3.1.8). Only cells that persisted through all rounds of 4i were included in subsequent analyses.

Random forest models

Two random forest (RF) models were trained to predict cell cycle age and phase (obtained by time lapse imaging) from the multivariate 4i signatures of the same cells. 80% of our annotated data was used to train the RF and the remaining 20% was reserved as a test set. Classification accuracy was used as the error metric to train the phase model, while root mean squared error (RMSE) was used to train the age model. The phase model yielded 95.5% accuracy (95% CI: 93.5, 0.971) and a kappa of 0.925. The age model had an RMSE of 125.8 with an R^2=0.862. Variable importance tables were obtained from each model (**fig. S2A, Table S2**) through calculation of unconditional permutation importance. All hyperparameter tuning was performed with 10-fold cross validation (Age: ntrees=500, mtry=246, Phase: ntrees=500, mtry=124).

To identify the optimal feature subset that best predicts the cell cycle state (i.e. age and phase), first a combined ranking was calculated for each feature as the average of the individual rankings from the variable importance tables obtained from the age and phase models. Successive random forest models were generated for both age and phase starting with a single feature and adding additional features in order of combined ranking. Accuracy (for cell cycle phase) or error (RMSE for cell cycle age) were calculated at each iteration (**fig. S2B-C**). The optimal feature was defined as the top 40 features (by combined ranking).

All RF analyses were performed using R (v1.2.5001) with caret (v6.0-86) and ggplot2 (v3.3.2) packages.

Convolutional neural network

The convolutional neural network (CNN) models predicting cell cycle phase and age were trained using as an input image stacks for individual cells extracted from 4i experiments (48 fluorescent channels and 4 channels of masks representing entire cell, cell nucleus, cytoplasm and cytoplasmic ring around the nucleus respectively; 52 frames total; 100 px x 100 px) and ground truth annotations obtained from the time lapse imaging. The Fastai (https://github.com/fastai/fastai) Python deep learning library was used for training and the initial pre-trained ResNet-50 convolutional networks were obtained directly from it. Both of the models were trained first using a low-resolution stack (50 px x 50 px) and then fine-tuned using full resolution stacks. The model predicting cell cycle phase was based on 2930 cells divided into a training set (2491 cells; 85%) and a validation set (439 cells, 15%). ResNet-50 CNN predicting phase was trained using a cross-entropy loss function. The model predicting cell cycle age was based on 2767 cells divided into a training set (2352 cells; 85%) and a validation set (415 cells, 15%). ResNet-50 CNN predicting age was trained using mean squared error loss function. Models were trained using Google Cloud VM (8 vCPUs, 52 GB memory, 1 x NVIDIA Tesla P100).

Manifold learning

Manifold learning was performed using Potential of Heat-diffusion for Affinity-based Transition Embedding (PHATE) (*29*) using the optimal feature set described above as input variables. PHATE was run on z-normalized variables with the following parameter sets: k-nearest neighbor

(knn)=200, t=12, gamma=1 for structures presented in **Figs. 1-4,** and knn=75, t=10, gamma=0.25 for structures presented in **Figs. 5-6**.

Data Visualization

Data were visualized using custom Python scripts (v3.7.1) in Jupyter Notebooks (v6.1.4), GraphPad Prism (v8) and scanpy (v1.6) (*53*). Scanpy was also used to prepare data for visualization in virtual reality using the singlecellVR website (singlecellvr.com) (*54*).

siRNA

RPE cells were treated with DMSO or etoposide (1 μM) for 24h then transfected with non-targeting (Dharmacon, D-001810-10-0) or cyclin D1/D2/D3 (SMARTPools L-003210-00-0005/L-003211-00-0005/L-003212-00-0005) siRNA pools using the DharmaFECT 1 transfection reagent (T-2001-01) as per manufacturer's protocol and incubated for 3 days prior to fixation. Immunofluorescence was performed as per the 4i protocol described above.

A

Feature	Gini	G2	Cyto	Overall Rank (raw)	Overall Rank	Final Rank
Int_Med_E2F1_nuc	20.84163	43.50332	80.76929	48.37141624	3	2.5
Int_Med_cycA_nuc	46.3729	61.24204	39.88589	49.16694049	2	3.5
Int_Med_cycD1_nuc	19.08683	40.63739	39.32977	33.01799819	4	4
Int_Med_p21_nuc	49.87202	24.68662	100	58.18621328	1	4.5
Int_Intg_DNA_nuc	30.83552	39.61428	11.97409	27.47463272	5	7
Int_Med_Skp2_nuc	19.81156	19.84781	25.3778	21.67905382	7	7
Int_Med_Cdt1_nuc	23.96836	11.11181	40.91351	25.33122514	6	9
AreaShape_Area_nuc	18.69789	15.39381	12.83393	15.64187816	9	10
Int_Med_Cdh1_nuc	10.18031	7.711686	10.24773	9.37990614	17	10
Int_Med_cycE_nuc	13.49548	6.691583	8.691987	9.626348478	15	10.5
Int_Med_PCNA_nuc	24.50459	1.646653	24.68011	16.9437846	8	10.5
Int_Med_pH2AX_nuc	14.29667	4.55838	13.56334	10.80612997	13	14.5
Int_Med_cMyc_nuc	8.111011	11.39421	8.777872	9.427697605	16	18.5
Int_Med_RB_nuc	8.670777	9.668571	5.605677	7.981675007	27	18.5
Int_Med_cycB1_cell	9.398394	17.14094	6.450245	10.9965248	12	19
Int_Med_cycB1_cyto	13.12189	15.43051	8.110295	12.2208971	11	19
Int_Med_cycB1_ring	14.40055	16.36057	9.628824	13.46331515	10	19
Int_Med_pRB_nuc	8.374246	9.25376	8.500841	8.709615665	20	21.5
Int_Med_cycB1_nuc	6.638866	11.54915	6.806072	8.331362607	23	22.5
Int_Med_p27_nuc	14.7056	9.488711	7.394393	10.52956838	14	22.5
Int_Med_ERK_nuc	6.526174	8.620578	8.302848	7.816533579	30	24.5
Int_Med_pp53_nuc	7.68274	5.180711	9.793377	7.552276063	34	26
Int_Med_S6_nuc	8.817886	6.538585	10.74766	8.701376516	21	30
Int_MeanEdge_cycB1_cell	3.730782	7.189864	10.1991	7.039914032	44	32
Int_Med_pp21_nuc	7.781977	7.995909	7.370322	7.716068937	31	32
Int_Med_CDK2_nuc	8.77473	8.97474	6.092366	7.947278769	28	32.5
Int_Med_CDK4_nuc	5.74308	4.004632	8.954497	6.234069766	65	33
Int_Med_DNA_nuc	4.835274	6.327453	9.530571	6.897766068	52	33
Int_Med_cFos_nuc	6.237598	2.449377	13.69261	7.459860782	36	37
AreaShape_Area_cell	4.549387	6.837163	9.600102	6.995550754	46	38
Int_MeanEdge_Fra1_cell	4.19064	11.78449	6.328584	7.434572682	37	38.5
Int_Med_CDK6_nuc	7.616113	5.822241	7.125466	6.854606831	53	38.5
Int_Med_p16_nuc	6.884546	5.536326	8.362765	6.927878822	49	42
Int_Med_cycD1_cyto	5.376849	6.224877	10.29345	7.298391931	38	46
Int_Med_GSK3b_nuc	7.991108	4.444278	8.454229	6.963204985	48	47
Int_Med_p38_nuc	6.051555	8.133543	8.276151	7.487082821	35	47
Int_Med_Bcl2_nuc	8.705268	5.342917	10.04676	8.031647466	26	48.5
Int_Med_CDK2_cyto	4.366365	6.364772	6.575736	5.768957921	84	49.5
Int_MeanEdge_Skp2_cell	7.041434	6.355065	8.076178	7.157558886	42	51.5
Int_Med_cycA_cell	6.490617	7.939731	8.23162	7.553989395	33	53

B

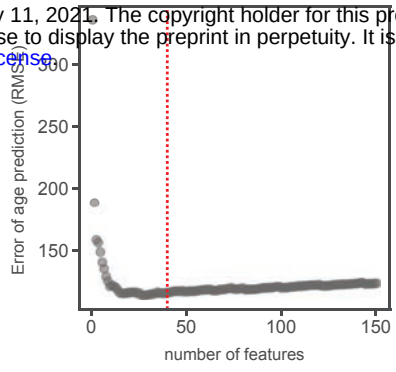

C

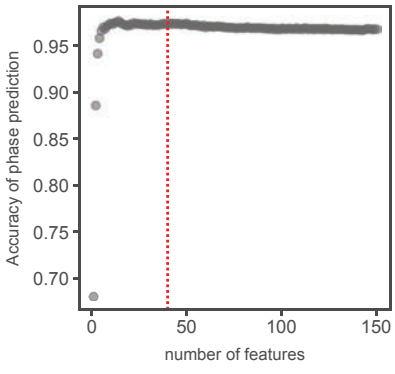

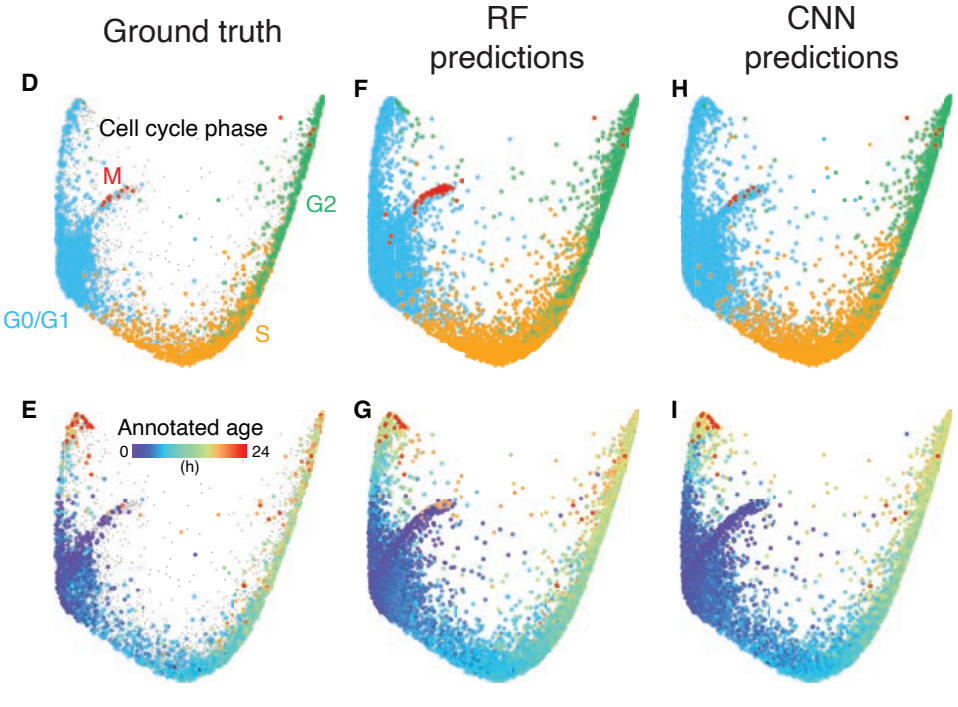

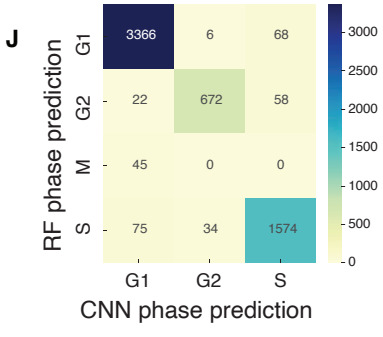

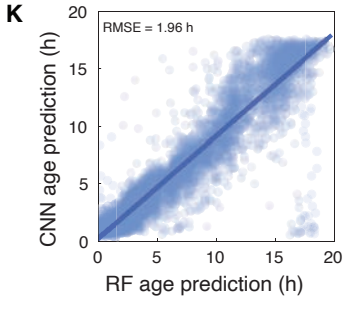

Figure S1 - Generation and annotation of the human cell cycle structure. (**A**) Random forest (RF) models were used to predict cell cycle age and phase annotations (obtained by time-lapse imaging) from the multivariate 4i signatures (see Methods). Variable importance tables were obtained that rank each feature by its importance in maximizing accuracy of phase predictions or reducing the error of age predictions (see full tables in Table 2). These rankings were averaged to obtain a combined rank for each feature. (**B-C**) Iterative random forest models were used to calculate prediction error for cell cycle age (B, RMSE: root mean squared error) and accuracy for phase (C) while increasing the number of features that were for training. Features were successively added in each iterative round, ordered by their combined rank as determined in A. Shown are iterations for the first 150 ranked features. The top 40 features were chosen as an optimal feature set and used as inputs for PHATE to generate the cell cycle structure. (**D-E**) Ground truth annotations of cell cycle phase (D) and age (E). (**F-G**) Random forest predictions of phase (F) and age (G) (same figures are presented in Fig. 1C-D, and are shown here for comparison). (**H-I**) Convolutional neural network (CNN) predictions of phase (F) and age (G). For panels F-I, phase and age ground truth annotations are also plotted on the structures. (**J**) Confusion matrix comparing RF and CNN phase predictions. The CNN model did not predict any M phase cells. (**K**) Concordance between RF and CNN predictions for age. Int: intensity; Med: median; nuc: nuclear; cyto: cytoplasm; ring: perinuclear area; MeanEdge: plasma membrane

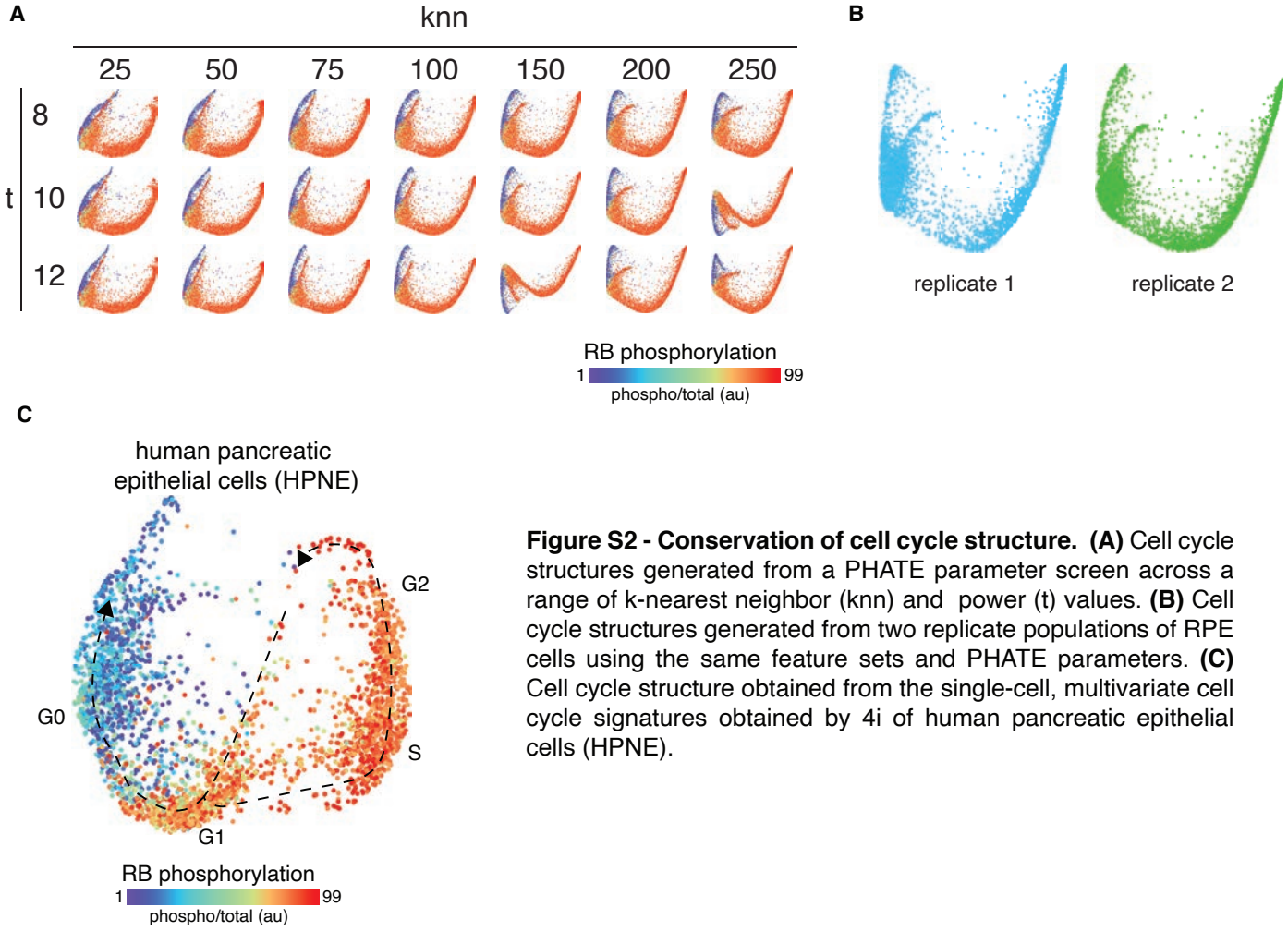

Figure S2 - Conservation of cell cycle structure. **(A)** Cell cycle structures generated from a PHATE parameter screen across a range of k-nearest neighbor (knn) and power (t) values. **(B)** Cell cycle structures generated from two replicate populations of RPE cells using the same feature sets and PHATE parameters. **(C)** Cell cycle structure obtained from the single-cell, multivariate cell cycle signatures obtained by 4i of human pancreatic epithelial cells (HPNE).

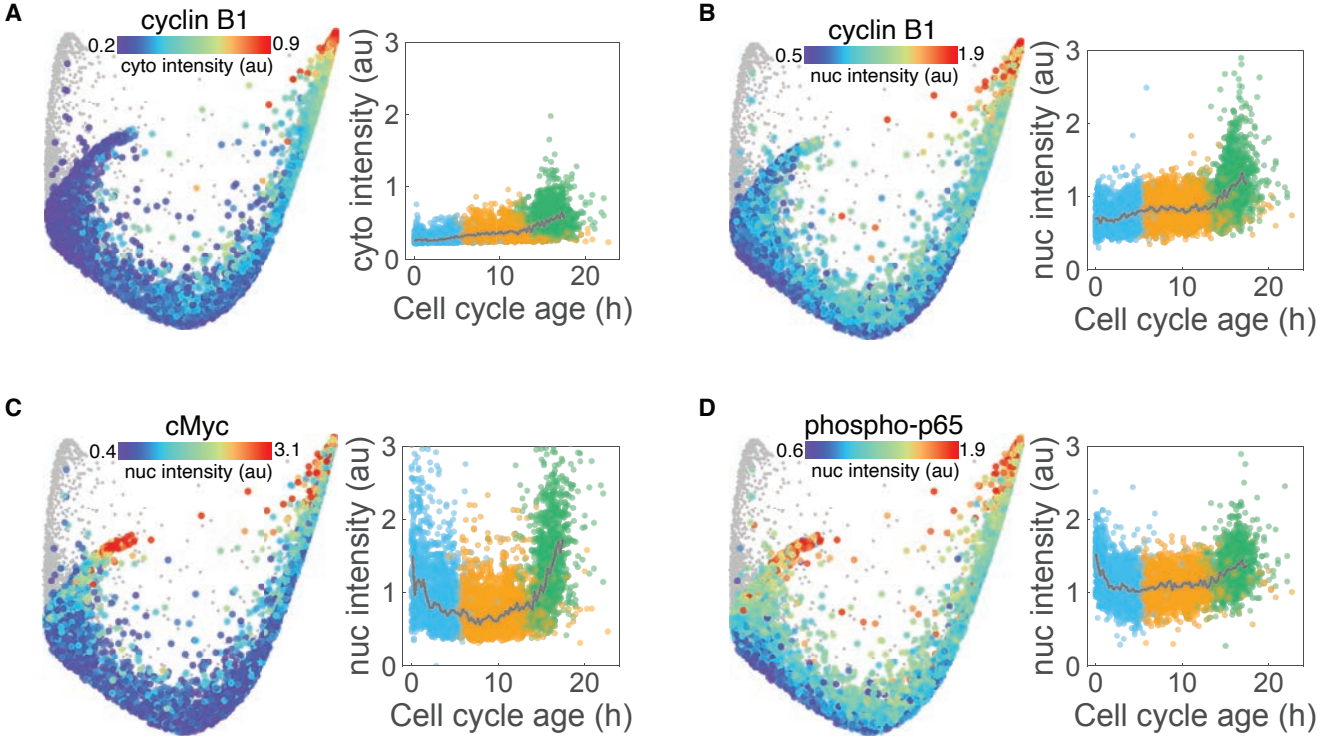

Figure S3 - Effector dynamics along the proliferative trajectory. Median cytoplasmic expression of cyclin B1 (A) and median nuclear expression of cyclin B1 (B), cMyc (C) and phospho-p65 (D) are mapped onto the proliferative trajectory of the cell cycle structure (left panels) and plotted against cell cycle age (right panels). Population medians in time courses indicated by solid grey lines and individual cells are colored by cell cycle phase (G1: blue, S: orange, G2: green). Non-cycling (G0) cells (phospho/total RB < 1.6) are shown in grey on the structure and are excluded from time courses.

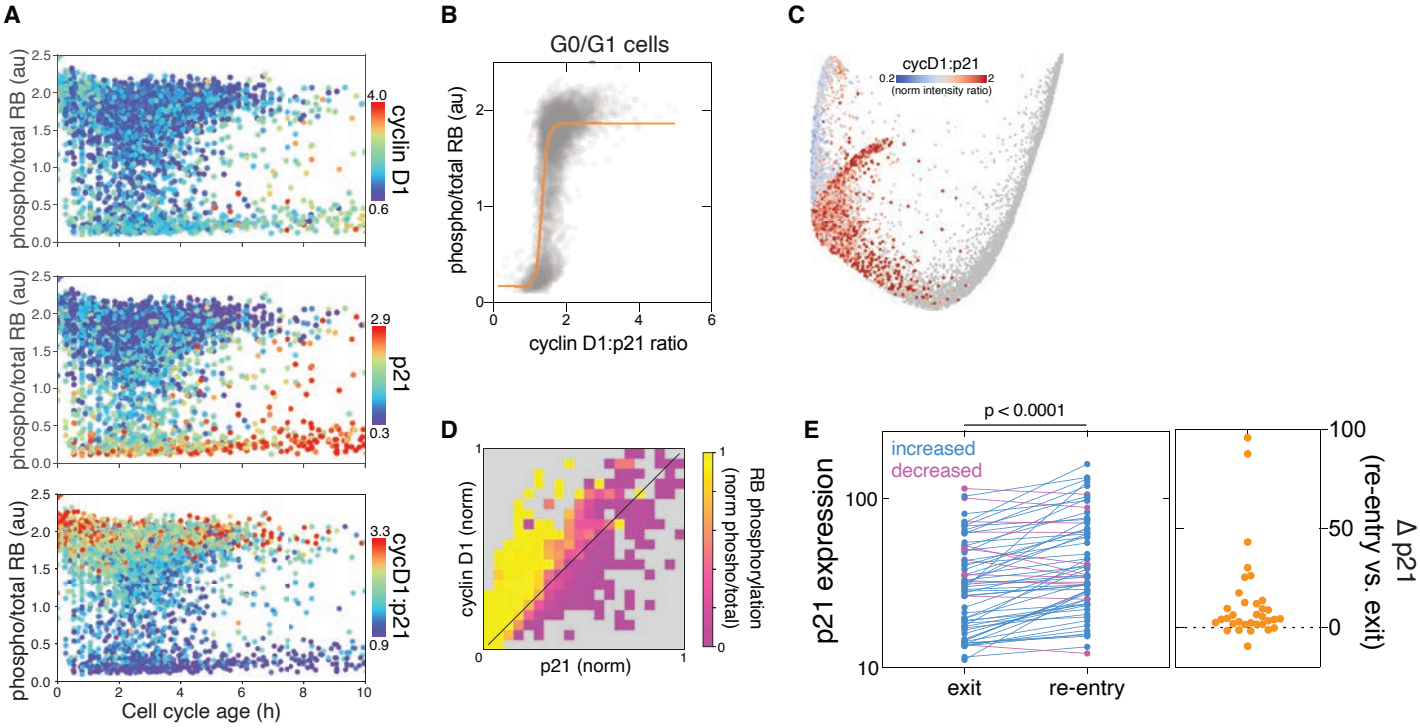

Figure S4 - The cyclin D1:p21 ratio regulates both cell cycle exit and re-entry. (**A**) Time courses of RB phosphorylation following mitosis are colored by median nuclear expression of cyclin D1 (upper panel) and p21 (middle panel) and the cyclin D1:p21 ratio (lower panel). Note the delay in RB dephosphorylation immediately following mitosis (<1h). (**B**) RB phosphorylation after cell division is controlled by the cyclin D1:p21 ratio in individual cells in an ultrasensitive manner (Hill coefficient = 12.2). Data from G0/G1 cells are shown. (**C**) The cyclin D1:p21 ratio of G0/G1 cells is mapped onto the cell cycle structure. Data is expressed as a z-normalized nuclear intensity ratio. (**D**) Heatmap showing the proportion of cells with high RB phosphorylation (phospho/total RB > 1.6) at a given ratio of z-normalized cyclin D1:p21 expression. (**E**) *Left panel*: Single cell p21 expression measured by time lapse imaging at the time of cell cycle exit (1h post-mitosis) versus re-entry (at time of CDK2 reactivation). *Right panel:* Difference in p21 expression at cell cycle re-entry versus exit. Statistical significance determined using a Student's paired *t* test. $N = 65$ cells.

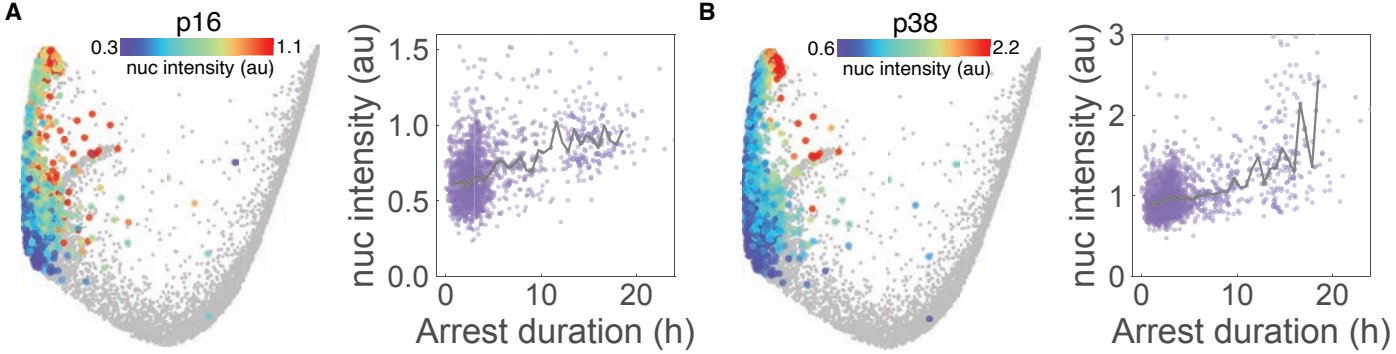

Figure S5 - Effector dynamics along the arrest trajectory. (**A-B**) Median nuclear expression of p16 (A) and p38 (B) are mapped onto the arrest trajectory of the cell cycle structure (left panels) and plotted against time of arrest (right panels). Population medians in time courses indicated by solid grey lines. Non-arrested cells (phospho/total RB > 1.6) are shown in grey on the structure and are excluded from time courses.

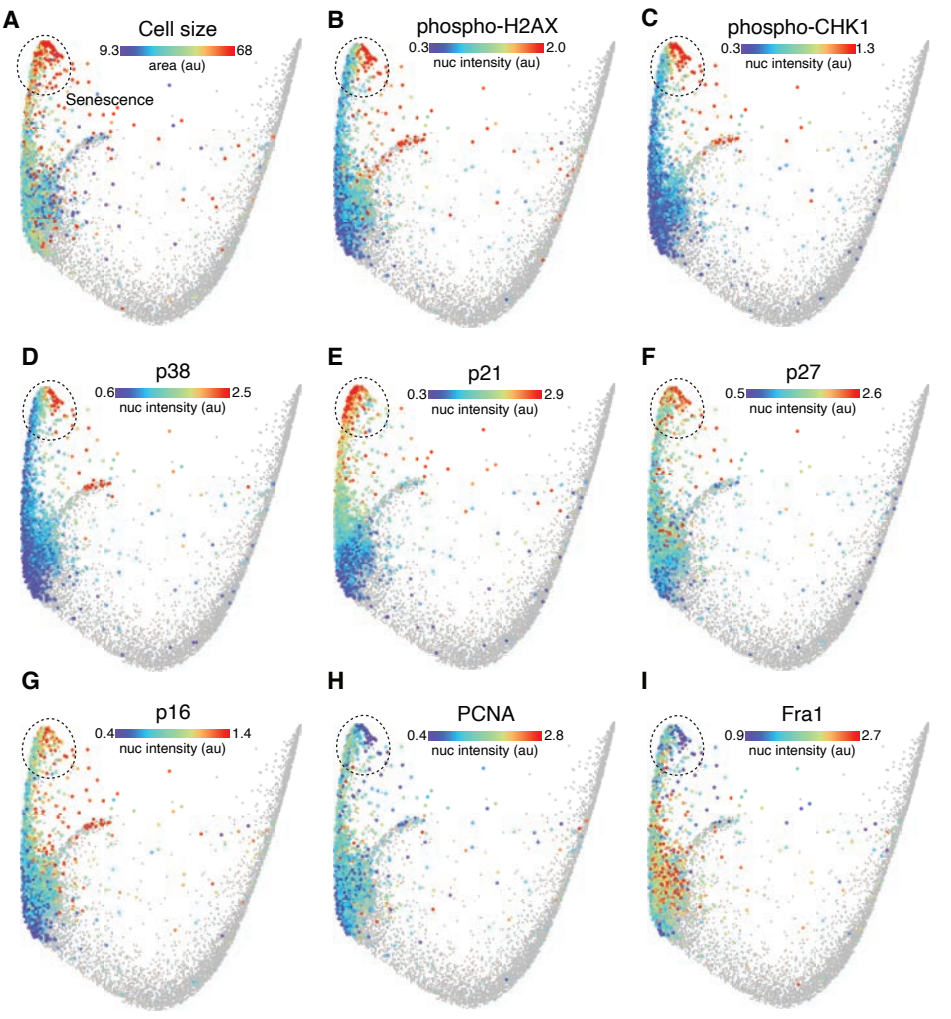

Figure S6 - Molecular signature of cellular senescence. **(A-I)** Cell size (A) and median nuclear intensities of phospho-H2AX (B), phospho-CHK1 (C), p38 (D), p21 (E), p27 (F), p16 (G), PCNA (H) and Fra1 (I) of arrested cells are mapped onto the cell cycle structure. Non-arrested cells (phospho/total RB > 1.6) are shown in grey.

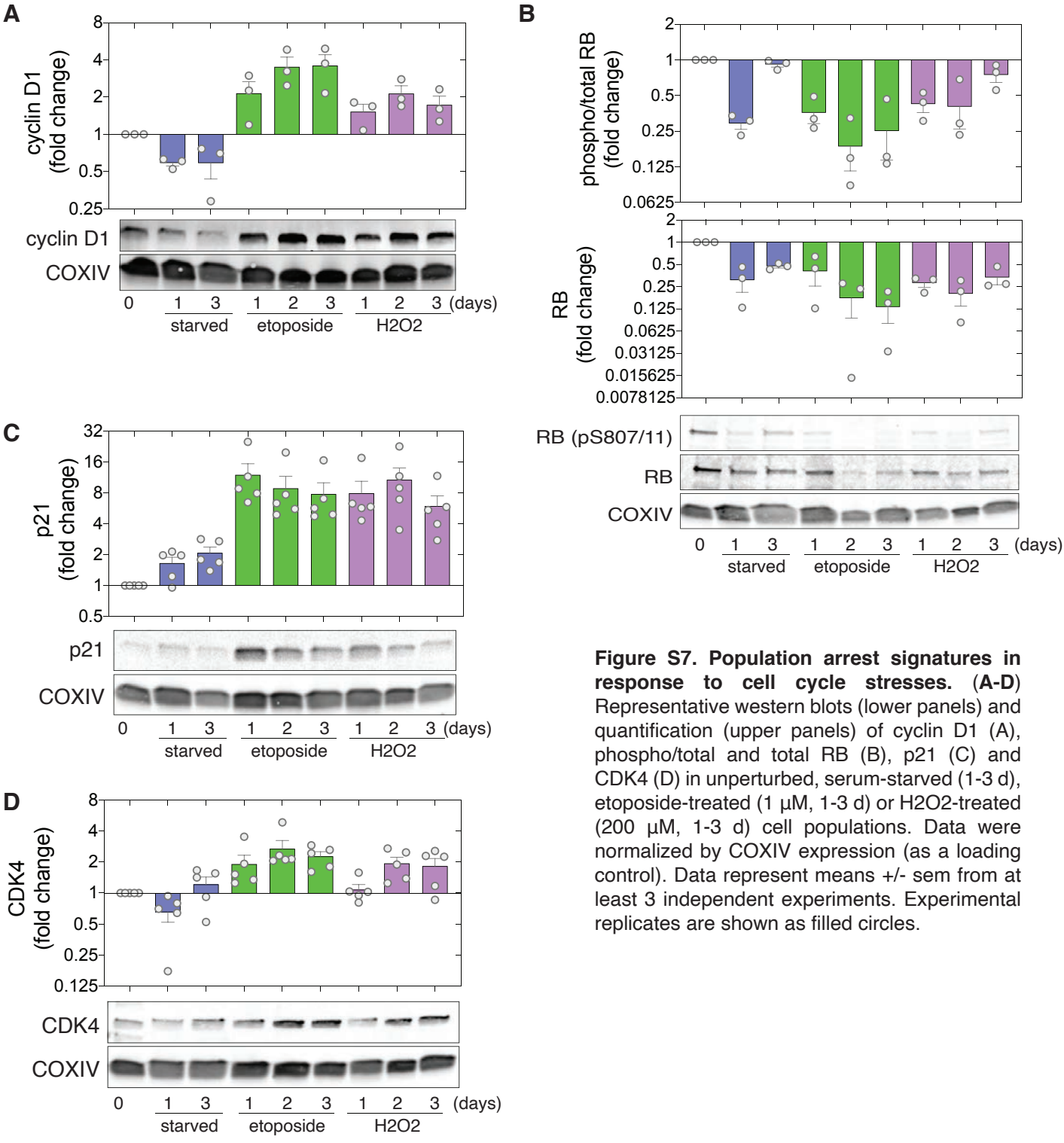

Figure S7. Population arrest signatures in response to cell cycle stresses. (**A-D**) Representative western blots (lower panels) and quantification (upper panels) of cyclin D1 (A), phospho/total and total RB (B), p21 (C) and CDK4 (D) in unperturbed, serum-starved (1-3 d), etoposide-treated (1 μM, 1-3 d) or H2O2-treated (200 μM, 1-3 d) cell populations. Data were normalized by COXIV expression (as a loading control). Data represent means +/- sem from at least 3 independent experiments. Experimental replicates are shown as filled circles.

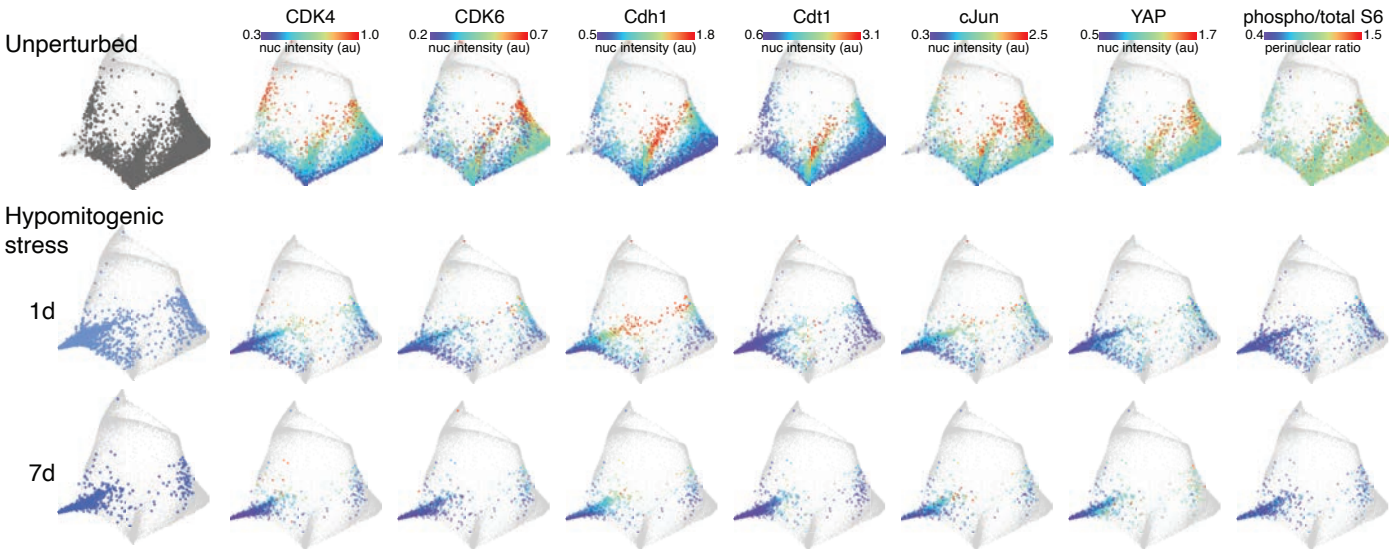

Figure S8 - Cell cycle signature of hypomitogenic stress. Median nuclear intensities of CDK4, CDK6, Cdh1, Cdt1, cJun and YAP, and perinucear S6 activation (phospho/total) are mapped onto unperturbed or serum-starved cells ("hypomitogenic stress", 1 or 7 days).

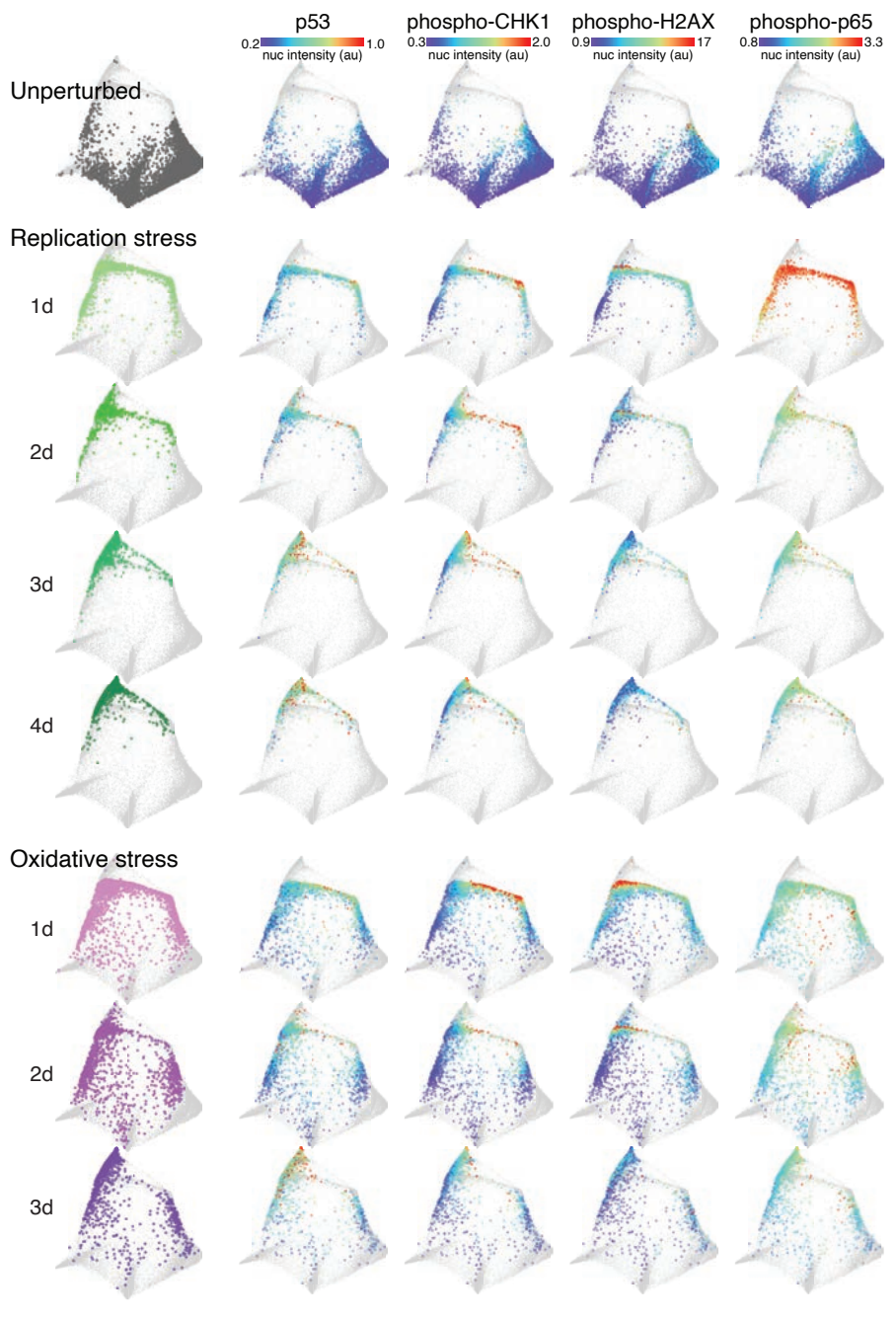

Figure S9 - Cell cycle signatures of replication and oxidative stress. Median nuclear intensities of p53, phospho-CHK1, phospho-H2AX and phospho-p65 are mapped onto unperturbed (grey), etoposide-treated (”replication stress”, 1 μM, 1-4 d) and H2O2-treated (”oxidative stress”, 200 μM, 1-3 d) cells.

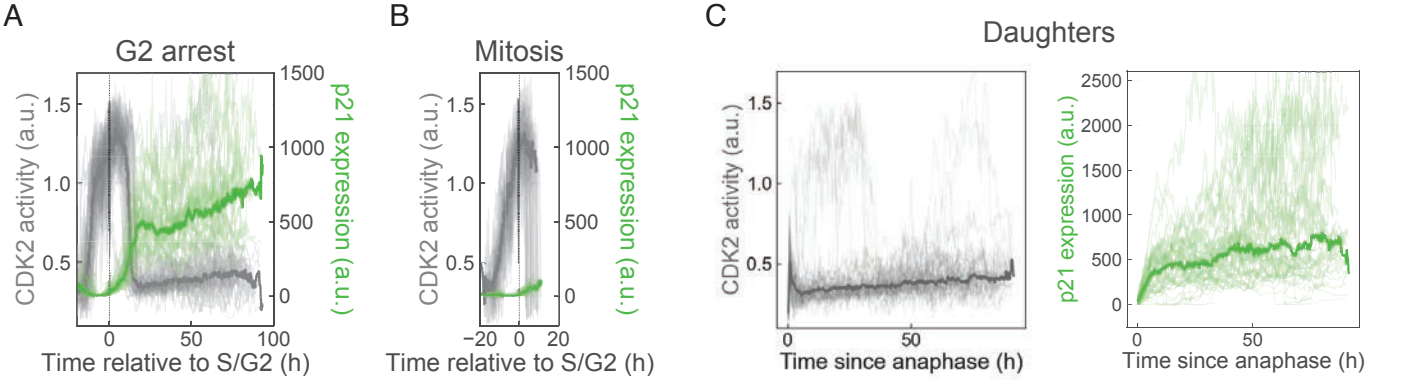

Figure S10. Time-lapse imaging of cell fate following etoposide treatment. (**A-B**) Single cell traces from time-lapse imaging of CDK2 activity (blue, quantified by the cytoplasm:nuclear ratio of DHB-mCherry) and p21-YPet expression (green) in cells undergoing G2 arrest (A) or mitosis (B) following etoposide treatment (1 μM) aligned at the S/G2 transition. (**C**) Single cell traces of the daughters of mitotic cells (from panel B). Thick lines represent population medians. These data are shown as heatmaps in Figure 5D-F. *N* = 117 cells

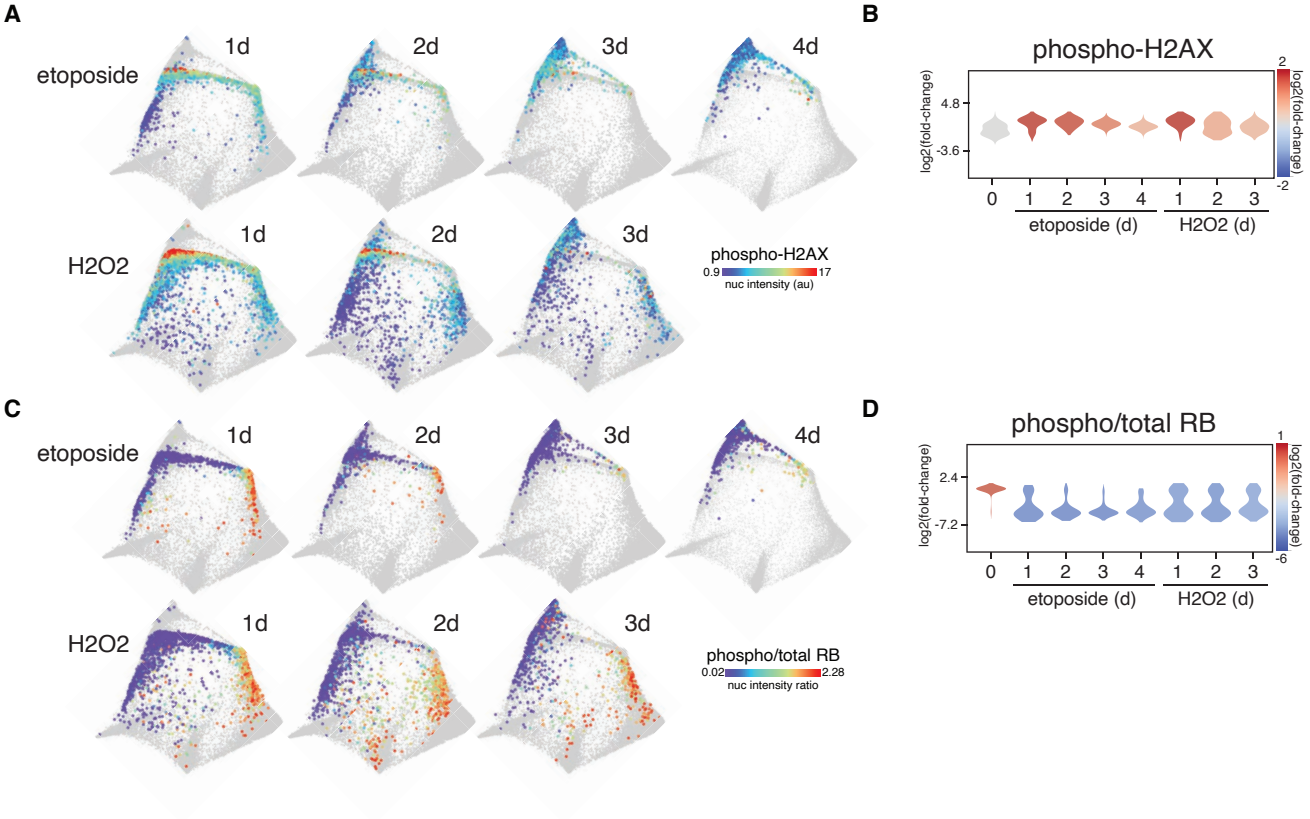

Figure S11 - Etoposide and H2O2 induce sustained and transient DNA damage responses, respectively. (**A-B**) Median nuclear phospho-H2AX intensity is mapped onto etoposide- and H2O2-treated cells (A) and plotted as single cell distributions (B). (**C-D**) RB phosphorylation (phospho/total) is mapped onto etoposide- and H2O2-treated cells (C) and plotted as single cell distributions (D).

5' homology arm (950bp, finishes just before stop codon):

GAGACAGGTGTCTTAACTCTGTTGGCCAGACTGGAGTGCAGTGATACGATCATGGCTCACTGCAGCTTCAAACTCCTGGGCTCAAGCGATCT
TCCTACCTCAGCCTCCTGGGTAGCTGGGAAGCTGGGACTATAGTTGTACACCACTACGCCCGGTTAATTTTTTGAGTTTTTGTAGAGACAAGG
TCTCACCATGTTGCCCGGGCTGGTCTTGAACTCCTGAGCTCAAGCAGTCCTCCTGCCTCAGCCTCCCAAAGTGTTGTGATTACAGGCGTGAGC
CACCATGCCCAGCCCCTTGCCATCCTTTTAGGGCAAGGAAACCAGGCTCAGAGAGGTAGAGTGATTTATCTAAGGTCTCAAAGTGAATTTGC
CGTTGGGTCAAGACTAATTATAATAACAACAACTACTGACGTTTATATGGGCCCGGCATTGTGCTGAACACTTTCATGGATTTTGTAACAGAA
TCCCTAGATCAGCACTGTCCAGTAACTCTGCAGGGATGGGAGTGTCCGGTACAGGGGCCACGAGCCACATACGGCTGTTGTGCATTTGACAC
ACAGCTCATGTGACTGAGGAACTGAATTGTTCATTTTATTTGATTGTAGTCTGTTTAAACAAGCACACAGAGCTAGTAGTGGTTCCTCTGCTG
GGCAGCTTGACTTAGAGCAGACCCATGGGTGCGGGTGCGGTGATGGATAAAATCACATCTGTGAAGCATGGTGGGACACTCCATAATACCCC
TCAAGAGACAGAGTGGACGTTCCCCGAGTTCTTCCTGTTCTCAGCAGTCGGCCCCATTGGCCCCAGGGAAGGGTGTCCTGGCCCCCCCACTGT
CTTCCTCAGTTGGGCAGCTCCGCCGCGTCCTCTTCTTCTTGGCCTGGCTGACTTCTGCTGTCTCTCCTCAGATTTCTACCACTCCAAACGCCGG
CTGATCTTCTCCAAGAGGAAGCCC

3' homology arm (900 bp, starts just after stop codon):

****Mutated PAM**

tccgcccacagCaagcctgcagtcctggaagcgcgagggcctcaaaggcccgctctacatcttctgccttagtctcagtttgtgtgtcttaattattatttgtgttttaatttaaacacct
cctcatgtacataccctggccgccccctgccccccagcctctggcattagaattatttaaacaaaaactaggcggttgaatgagaggttcctaagagtgctgggcatttttatttttatg
aaatactatttaaagcctcctcatcccgtgttctccttttcctctctcccggaggttgggtgggccggcttcatgccagctacttcctcctccccacttgtccgctgggtggtaccctctg
gaggggtgtggctccttcccatcgctgtcacaggcggttatgaaattcacccccttttcctggacactcagacctgaattctttttcatttgagaagtaaacagatggcactttgaaggg
gcctcaccgagtgggggcatcatcaaaaactttggagtcccctcacctcctctaaggttgggcagggtgaccctgaagtgagcacagcctagggctgagctggggacctggtac
cctcctggctcttgataccccccctctgtcttgtgaaggcagggggaaggtggggtcctggagcagaccaccccgcctgccctcatggcccctctgacctgcactggggagcccgtc
tcagtgttgagccttttccctctttggctcccctgtacctttttgaggagccccagctacccttttttctccagctgggctctgcaattcccctctgctgctgtccctccccctttgtcctttccctt
cagtaccctctcagctccaggtggctctgaggtgcctgtcccacccccacccccagctcaatgga

INSERT 1:

Ypet/P2A/neoR

ggagctggtgcaggcgctggagccggtgccgtgagcaaaggcgaagagctgttcaccggcgtggtgcccatcctggtggagctggacggcgacgtgaacggccacaagtt
cagcgtgagcggcgagggcgagggcgacgccacctacggcaagctgaccctgaagctgctgtgcaccaccggcaagctgcccgtgccctggcccaccctggtgaccaccc
tgggctacggcgtgcagtgcttcgcccggtaccccgaccacatgaagcagcacgacttcttcaagagcgccatgcccgagggctacgtgcaggagcggaccatcttcttcaa
ggacgacggcaactacaagacccgggccgaggtgaagttcgagggcgacaccctggtgaaccggatcgagctgaagggcatcgacttcaaggaggacggcaacatcctg
ggccacaagctggagtacaactacaacagccacaacgtgtacatcaccgccgacaagcagaagaacggcatcaaggccaacttcaagatccggcacaacatcgaggacgg
cggcgtgcagctggccgaccactaccagcagaacaccccatcggcgacggccccgtgctgctgcccgacaaccactacctgagctaccagagcgccctgttcaaggacccc
aacgagaagcgggaccacatggtgctgctggagttcctgaccgccgccggcatcaccgagggcatgaacgagctctataagGGAAGCGGAGCTACTAACTTCAGC
CTGCTGAAGCAGGCTGGAGACGTGGAGGAGAACCCTGGACCTatgattgaacaagatggattgcacgcaggttctccggccgcttgggtggagaggctattc
ggctatgactgggcacaacagacaatcggctgctctgatgccgccgtgttccggctgtcagcgcaggggcgcccggttctttttgtcaagaccgacctgtccggtgccctgaat
gaactgcaagacgaggcagcgcggctatcgtggctggccacgacgggcgttccttgcgcagctgtgctcgacgttgtcactgaagcgggaagggactggctgctattgggc
gaagtgccggggcaggatctcctgtcatctcaccttgctcctgccgagaaagtatccatcatggctgatgcaatgcggcggctgcatacgcttgatccggctacctgcccattcg
accaccaagcgaaacatcgcatcgagcgagcacgtactcggatggaagccggtcttgtcgatcaggatgatctggacgaagagcatcaggggctcgcgccagccgaactgt
tcgccaggctcaaggcgagcatgcccgacggcgaggatctcgtcgtgacccatggcgatgcctgcttgccgaatatcatggtggaaaatggccgcttttctggattcatcgact
gtggccggctgggtgtggcggaccgctatcaggacatagcgttggctacccgtgatattgctgaagagcttggcggcgaatgggctgaccgcttcctcgtgctttacggtatc
gccgctcccgattcgcagcgcatcgccttctatcgccttcttgacgagttcttctga

Figure S12: Donor cassette used to generate p21-YPet gene by CRISPR-Cas9-mediated knock-in

Table S1. Antibodies

Primary Antibodies

Target	Host species	Dilution	Supplier	Catalog#	Published citations	Published figures
53BP1	Rb	1:1000	Santa Cruz	sc-22760	114	207
Akt	Ms	1:100	CST	2920	397	649
Bcl-2	Rb	1:200	CST	2827	38	60
beta-catenin	Ms	1:200	CST	2677	39	82
c-Fos	Rb	1:200	CST	2250	81	124
c-Jun	Rb	1:400	CST	9165	356	620
c-Myc	Rb	1:500	CST	5605	402	
cdc6	Ms	1:100	Santa-Cruz	sc-9964	33	88
Cdh1	Ms	1:100	Santa Cruz	sc-56312	6	8
CDK2	Gt	1:500	R&D	AF4654	2	2
Cdk6	Rb	1:250	abcam	ab124821	19	30
CDK6	Rb	1:250	abcam	ab124821	19	30
Cdt1	Rb	1:200	CST	8064	9	28
Cyclin A	Ms	1:50	Santa Cruz	sc-271682	13	18
cyclin B1	Gt	1:100	R&D	AF6000	41	52
cyclin D1	Ms	1:100	Santa Cruz	sc-20044	115	190
cyclin E	Ms	1:50	Santa Cruz	sc-247	47	66
E2F1	Ms	1:100	Santa Cruz	sc-251	146	273
ERK	Ms	1:100	CST	4696	132	181
Fra1	Ms	1:100	Santa Cruz	sc-28310	23	70
GSK3b	Ms	1:100	CST	9832	64	113
GSK3b	Ms	1:100	CST	9832	64	113
p16	Rb	1:400	abcam	ab108349	40	62
p21	Gt	1:200	R&D	AF1047	7	18
p27	Rb	1:800	CST	3686	58	85
p38	Rb	1:100	CST	8690	426	573
p53	Ms	1:400	CST	48818	12	23
PCNA	Ms	1:500	CST	2586	193	286
phospho-Akt (Ser473)	Rb	1:200	CST	4060	2700	4300
phospho-Bcl2	Ms	1:200	CST	15071	159	220
phospho-cdc6 (Ser54)	Rb	1:200	abcam	ab75809	3	12
phospho-cdc6 (Ser54)	Rb	1:200	abcam	ab75809	4	13
phospho-CHK1 (S317)	Rb	1:800	CST	12302	17	30
phospho-ERK (T202/Y204)	Rb	1:200	CST	4370	1600	2300
phospho-H2AX (S139)	Ms	1:200	CST	80312	3	3
phospho-p21 (T145)	Rb	1:1000	abcam	ab47300	2	4
phospho-p27 (T157)	Rb	1:60	abcam	ab85047	5	5
phospho-p38 (T180/Y182)	Ms	1:200	CST	9216	158	250
phospho-p53 (S15)	Ms	1:400	CST	9286	87	145
phospho-p65 (S536)	Ms	1:100	CST	3036	32	44
phospho-RB	Rb	1:1000	CST	8516	48	70
phospho-Rsk (S380)	Rb	1:500	CST	11989	13	25
phospho-S6 (S235/236)	Rb	1:200	CST	4858	156	250
phospho-STAT3 (Y705)	Rb	1:100	CST	9145	1000	1700
RB	Ms	1:500	CST	9309	123	180
Rsk1	Ms	1:50	R&D	MAB992		
S6	Ms	1:100	CST	2317	107	152
Skp2	Rb	1:800	CST	2652	20	47
SMAD2	Ms	1:200	abcam	ab119907	3	8
STAT3	Ms	1:500	CST	9139	551	1000
YAP	Ms	1:50	Santa Cruz	sc-101199	55	129

Secondary Antibodies

Host/target species	Fluorophore	Dilution	Supplier	Catalog#
Donkey anti-rabbit	AlexaFluor Plus 488	1:500	ThermoFisher	A32790
Donkey anti-mouse	AlexaFluor Plus 555	1:500	ThermoFisher	A32773
Donkey anti-rabbit	AlexaFluor Plus 647	1:500	ThermoFisher	A32773
Donkey anti-goat	AlexaFluor Plus 647	1:500	ThermoFisher	A32758

Table S2. Variable importance for cell cycle phase and age determined by random forest modeling.

	Phase predictions					Age predictions		Combined
Feature	G1	G2	S	Avg. Accuracy	Rank (phase)	Overall	Rank (age)	rank
Int_Med_E2F1_nuc	20.8416345	43.5033153	80.769287	48.37141224	3	87.5513848	2	2.5
Int_Med_cycA_nuc	46.3728974	61.2420373	39.8858868	49.16694049	2	66.5187946	5	3.5
Int_Med_cycD1_nuc	19.0868267	40.6373948	39.329773	33.01799819	4	70.0099297	4	4
Int_Med_p21_nuc	49.8720167	24.6866232	100	58.18621328	1	52.0268976	8	4.5
Int_Intg_DNA_nuc	30.8355211	39.6142844	11.9740926	27.47463272	5	50.8467038	9	7
Int_Med_Skp2_nuc	19.8115563	19.8478071	25.3777981	21.67905382	7	53.3960404	7	7
Int_Med_Cdt1_nuc	23.9683558	11.1118082	40.9135115	25.33122514	6	42.5777069	12	9
AreaShape_Area_nuc	18.6978933	15.3938072	12.833934	15.64187816	9	42.8525874	11	10
Int_Med_Cdh1_nuc	10.1803055	7.71168631	10.2477266	9.37990614	17	74.6759305	3	10
Int_Med_cycE_nuc	13.4954759	6.69158295	8.69198661	9.626348478	15	63.2481896	6	10.5
Int_Med_PCNA_nuc	24.5045904	1.64665321	24.6801102	16.9437846	8	42.1294723	13	10.5
Int_Med_pH2AX_nuc	14.2966746	4.55838021	13.5633351	10.80612997	13	28.3966588	16	14.5
Int_Med_cMyc_nuc	8.1110109	11.3942101	8.77787183	9.427697605	16	23.5218891	21	18.5
Int_Med_RB_nuc	8.67077701	9.66857124	5.60567678	7.981675007	27	49.5896932	10	18.5
Int_Med_cycB1_cell	9.39839377	17.1409352	6.45024545	10.9965248	12	20.4502255	26	19
Int_Med_cycB1_cyto	13.1218876	15.4305086	8.11029514	12.2208971	11	20.0013589	27	19
Int_Med_cycB1_ring	14.4005477	16.3605739	9.62882386	13.46331515	10	19.2817017	28	19
Int_Med_pRB_nuc	8.37424602	9.25375976	8.50084121	8.709615665	20	21.6417528	23	21.5
Int_Med_cycB1_nuc	6.63886604	11.5491499	6.80607184	8.331362607	23	22.9032525	22	22.5
Int_Med_p27_nuc	14.7056012	9.48871114	7.3943928	10.52956838	14	16.9040662	31	22.5
Int_Med_ERK_nuc	6.52617417	8.62057819	8.30284838	7.816533579	30	24.5353473	19	24.5
Int_Med_pp53_nuc	7.68273962	5.18071131	9.79337726	7.552276063	34	27.7968987	18	26
Int_Med_S6_nuc	8.81788582	6.53858523	10.7476585	8.701376516	21	14.6451815	39	30
Int_MeanEdge_cycB1_cell	3.73078155	7.18986437	10.1990962	7.039914032	44	23.5535044	20	32
Int_Med_pp21_nuc	7.78197655	7.99590876	7.3703215	7.716068937	31	16.559943	33	32
Int_Med_CDK2_nuc	8.77473047	8.97474017	6.09236567	7.947278769	28	15.08775	37	32.5
Int_Med_CDK4_nuc	5.74308022	4.00463208	8.95449699	6.234069766	65	100	1	33
Int_Med_DNA_nuc	4.83527387	6.32745304	9.53057129	6.897766068	52	34.5077264	14	33
Int_Med_cFos_nuc	6.23759789	2.449377	13.6926075	7.459860782	36	15.0815855	38	37
AreaShape_Area_cell	4.54938694	6.83716331	9.60010201	6.995550754	46	17.4047086	30	38
Int_MeanEdge_Fra1_cell	4.19063977	11.7844947	6.32858356	7.434572682	37	14.0805859	40	38.5
Int_Med_CDK6_nuc	7.61611298	5.82224141	7.1254661	6.854606831	53	21.5721082	24	38.5
Int_Med_p16_nuc	6.88454556	5.53632573	8.36276517	6.927878822	49	15.7916665	35	42
Int_Med_cycD1_cyto	5.37684871	6.22487698	10.2934501	7.298391931	38	11.4455939	54	46
Int_Med_GSK3b_nuc	7.99110801	4.44427811	8.45422884	6.963204985	48	12.8624942	46	47
Int_Med_p38_nuc	6.05155472	8.13354268	8.27615107	7.487082821	35	11.1075572	59	47
Int_Med_Bcl2_nuc	8.7052681	5.34291656	10.0467577	8.031647466	26	10.4158409	71	48.5
Int_Med_CDK2_cyto	4.36636515	6.36477219	6.57573643	5.768957921	84	28.8223804	15	49.5
Int_MeanEdge_Skp2_cell	7.04143351	6.35506549	8.07617766	7.157558886	42	10.9755199	61	51.5
Int_Med_cycA_cell	6.49061655	7.93973126	8.23162037	7.553989395	33	10.2659049	73	53
Int_Med_Skp2_cell	5.06564797	7.28077216	6.64066972	6.329029953	62	13.3158247	44	53
Int_Med_cycA_ring	4.7072464	11.0117945	6.08371573	7.26758554	39	10.5031208	68	53.5
Int_Med_cycD1_cell	3.66842769	8.87091104	11.1857423	7.908360326	29	10.1566141	79	54
Int_Med_pp65_nuc	8.24126107	4.6945328	6.4459245	6.46057279	60	11.8991068	50	55
Int_Med_YAP_nuc	6.57874405	4.76805207	6.65588469	6.000893603	76	15.9063927	34	55
Int_Med_pSTAT3_nuc	6.35781231	7.75013317	5.46316665	6.523704042	58	11.4392693	55	56.5
Int_Med_CDK2_cell	4.97948786	6.10639062	6.10166603	5.729181503	86	15.4145382	36	61
Int_Med_E2F1_cell	4.62147023	6.55564375	7.05300851	6.076707496	73	11.5666636	52	62.5
Int_Med_pGSK3b_nuc	9.46468705	7.86563447	3.69401886	7.008113461	45	10.1513281	80	62.5
AreaShape_Area_cyto	6.75350852	4.66556693	6.65470241	6.024592618	74	11.3902334	56	65
AreaShape_FormFactor_nuc	5.27101733	9.6051853	1.19738791	5.357863512	105	17.7482023	29	67
Int_MeanEdge_DNA_cell	4.54358462	7.25423138	5.87960634	5.892474114	80	11.2468189	57	68.5
Int_Med_p53_nuc	7.45846106	4.79673543	5.77162244	6.008939641	75	10.8214916	63	69
Int_Med_pCHK1_nuc	5.94525798	4.17416396	10.6399931	6.919805019	51	9.50623512	93	72
Int_MeanEdge_cycE_cell	3.63708658	6.40990171	6.05954884	5.368845708	103	13.5735753	42	72.5
Int_MeanEdge_CDK2_cell	4.35611294	5.17004884	6.56326344	5.363141741	104	13.5227483	43	73.5

Int_MeanEdge_cMyc_cell	4.22529655	5.92401759	10.7467114	6.965341844	47	9.23682726	101	74
Int_Med_pAKT_cell	5.17812708	3.87406395	7.05706321	5.369751411	102	11.484562	53	77.5
Int_Med_Cdt1_ring	5.9521051	5.79920467	5.07945883	5.610256197	90	10.5555153	67	78.5
Int_Med_Cdh1_ring	5.9330145	5.96853884	11.1365044	7.679352564	32	8.43466609	126	79
Int_Med_pERK_cell	6.51798426	3.12208916	9.14052815	6.260200525	63	9.3959302	96	79.5
Int_Med_cycA_cyto	4.96377164	9.31957516	6.25772045	6.847022416	54	9.05037953	107	80.5
Int_MeanEdge_cJun_cell	5.74403861	3.78371395	6.82868997	5.45214751	98	10.7445299	65	81.5
Int_MeanEdge_pp38_cell	6.66251776	4.55746382	7.48246312	6.234148232	64	9.26971093	99	81.5
Int_Med_pp38_nuc	8.46471126	4.84074875	7.05941973	6.788293246	56	8.96558808	109	82.5
Int_MeanEdge_pERK_cell	2.83425787	5.60210364	8.48217977	5.639513763	89	10.1801604	78	83.5
Int_MeanEdge_YAP_cell	4.59419732	3.25230938	9.40963482	5.752047173	85	9.93828414	84	84.5
Int_MeanEdge_pS6_cell	5.42874488	5.03985237	5.95542035	5.474672535	95	10.231439	75	85
Int_Med_E2F1_cyto	5.9210212	6.27642164	4.13435121	5.443931349	100	10.45552	70	85
Int_MeanEdge_p53_cell	2.66098798	6.98682717	10.2213628	6.623059331	57	8.73905916	114	85.5
Int_MeanEdge_p38_cell	4.86149909	5.98147056	4.48858156	5.110517071	121	11.6230197	51	86
Int_Med_cycD1_ring	4.59148968	7.18343488	9.59618306	7.123702539	43	8.08670145	130	86.5
Int_Med_PCNA_cyto	4.5739036	6.44458989	13.2567481	8.091747181	24	7.32693735	153	88.5
Int_Med_p14ARF_cyto	3.63392254	6.65644519	8.28538689	6.191918204	67	8.84423465	111	89
Int_Med_BP1_nuc	4.47277406	3.41973708	6.84553932	4.912683483	133	12.4127534	48	90.5
Int_Med_E2F1_ring	6.06578286	6.09800518	5.15522253	5.773003524	83	9.37792654	98	90.5
Int_Med_pERK_nuc	5.15367033	4.54652374	4.16006796	4.620087343	157	20.6550067	25	91
Int_Med_cJun_cell	5.3510828	3.92630642	6.4723069	5.249898705	112	10.319593	72	92
Int_Med_p16_ring	4.63845967	5.14147168	5.13893474	4.97295536	127	11.2242694	58	92.5
Int_Med_Fra1_nuc	5.46554351	4.53472249	3.93876957	4.646345192	155	16.7603789	32	93.5
Int_Med_Skp2_cyto	4.57655962	5.47766769	7.35624283	5.803490046	81	9.06871679	106	93.5
Int_Med_Cdh1_cyto	7.08923521	6.7448382	11.519171	8.451081482	22	6.96168471	167	94.5
Int_Med_CDK2_ring	3.48215689	3.56482628	6.30235351	4.449778893	172	28.2967074	17	94.5
Int_Med_CDK6_cyto	4.28469037	6.0612052	6.67583668	5.673910752	87	9.19657132	103	95
Int_Med_bCat_nuc	7.00138567	5.49494376	7.90854837	6.801625934	55	7.93835617	136	95.5
Int_MeanEdge_bCat_cell	4.2345368	4.66450649	6.11639039	5.005144559	126	10.7371318	66	96
Int_Med_Cdt1_cyto	5.13341407	7.37490282	3.86943615	5.459251013	97	9.39648543	95	96
Int_Med_cJun_nuc	5.36661604	5.93158832	7.0314396	6.109881321	72	8.59920941	120	96
Int_Med_Cdh1_cell	6.24645955	6.40849529	13.6139332	8.756296024	19	6.65042438	175	97
Int_Med_pAKT_nuc	4.40815871	3.50612049	16.2958563	8.070045177	25	6.92043686	169	97
Int_MeanEdge_AKT_cell	4.87638099	1.55135007	7.37187736	4.599869471	160	13.6349856	41	100.5
Int_Med_PCNA_ring	4.65554456	4.54622655	12.337283	7.179684689	41	7.13270871	162	101.5
Int_MeanEdge_E2F1_cell	5.61218155	3.26095071	6.19990685	5.024346368	125	10.1376051	81	103
Int_Med_pS6_cell	3.56092436	6.47905802	5.31161298	5.11719845	120	9.77259619	87	103.5
Int_Med_cMyc_cell	6.67312879	8.61303868	11.7085569	8.998241471	18	6.08795095	190	104
Int_Med_cMyc_cyto	5.33898415	5.62332443	7.52441586	6.162241481	68	7.7443868	140	104
Int_Med_p14ARF_cell	2.80295897	4.95992609	8.45644621	5.406443755	101	9.03880392	108	104.5
Int_Med_pS6_cyto	3.44010879	5.89283955	6.07444705	5.135798462	117	9.42100799	94	105.5
Int_MeanEdge_pGSK3b_cell	5.13957901	3.99983468	10.2458806	6.461764774	59	7.3201272	154	106.5
Int_Med_ERK_cell	4.27811959	5.82135676	7.89811265	5.999196332	77	7.9038497	137	107
Int_MeanEdge_CDK4_cell	3.79646066	5.60410718	7.25467935	5.551749061	93	8.56488294	122	107.5
Int_Med_pGSK3b_cell	4.89397266	5.56104611	6.21019471	5.555071161	92	8.55083563	123	107.5
Int_Med_Skp2_ring	4.08574567	6.72184598	7.67671544	6.161435698	69	7.60996531	147	108
Int_Med_p16_cell	4.57651451	4.6920423	5.23776743	4.835441412	140	9.88456305	85	112.5
Int_MeanEdge_pp27_cell	3.39012726	5.94023143	7.46147431	5.597277665	91	7.95177856	135	113
Int_MeanEdge_ERK_cell	4.7213778	5.46809084	2.90467256	4.364713733	182	13.1188493	45	113.5
Int_Med_bCat_cell	3.82236268	4.10410644	6.22743986	4.717969659	151	10.2225656	76	113.5
Int_Med_pERK_ring	3.76120665	3.68104118	6.83458404	4.758943957	147	9.94654262	82	114.5
Int_MeanEdge_GSK3b_cell	4.27374594	4.91367191	4.80565465	4.6643575	153	10.2013233	77	115
Int_Med_GSK3b_ring	3.44015186	4.33862151	8.04180882	5.273527397	111	8.58407044	121	116
Int_Med_p53_ring	5.86437006	4.49633544	5.00739978	5.12270176	119	8.7552802	113	116
Int_Med_AKT_cell	5.0644557	5.16210047	5.8339104	5.353488856	106	8.39963613	127	116.5
Int_Med_p14ARF_nuc	3.57001145	11.8348029	5.36299323	6.922602526	50	6.4426703	184	117
Int_Med_pp53_ring	5.17725147	6.00274978	5.15302132	5.444340855	99	7.52440229	148	123.5
Int_Med_S6_cell	5.33841665	5.2239114	4.81066278	5.124330276	118	8.23163267	129	123.5
Int_Med_pAKT_ring	4.4642971	4.43223706	5.84720719	4.914580445	131	8.63964443	117	124

Int_Med_p38_cyto	4.21218859	5.72156939	3.83029552	4.588017832	162	9.69398684	89	125.5
Int_Med_CDK4_cell	2.6756964	4.80307861	6.65140273	4.710059246	152	9.25020287	100	126
Int_Med_PCNA_cell	5.00777224	1.85264554	11.0596457	5.973354484	78	6.67507795	174	126
Int_Med_pS6_ring	2.17947852	3.73381803	6.05889337	3.990729971	206	12.8023457	47	126.5
Int_Med_RB_cell	6.40478663	4.80295541	6.6691454	5.958962478	79	6.65000691	176	127.5
Int_Med_p14ARF_ring	6.40969156	3.72013953	5.4360496	5.188626896	115	7.7195998	141	128
Int_Med_pRB_cyto	5.34060335	3.02884969	3.7732211	4.047558046	199	10.985201	60	129.5
Int_Med_p16_cyto	5.1653596	3.84412808	4.33753564	4.449007774	173	9.70395335	88	130.5
Int_Med_Cdt1_cell	2.35941779	9.11382386	1.32446207	4.265901242	188	10.2482525	74	131
Int_Med_GSK3b_cell	4.55240645	4.15883787	5.6053742	4.772206175	145	8.61350898	118	131.5
Int_Med_p38_cell	3.96163996	6.71904049	4.94600096	5.208893803	114	7.49393418	149	131.5
Int_MeanEdge_Cdt1_cell	1.57987416	5.66039391	6.55037025	4.596879439	161	9.17776908	104	132.5
Int_Med_BP1_cell	6.88963114	5.74594169	4.31348137	5.649684732	88	6.5933352	177	132.5
Int_MeanEdge_cycA_cell	3.17654747	6.71026981	4.58433582	4.8237177	141	8.45954916	125	133
Int_Med_Fra1_cell	5.10285663	2.90039033	6.6017487	4.868331883	138	8.36797175	128	133
Int_Med_DNA_ring	3.80507745	4.93387186	5.96823152	4.902393613	135	7.98283801	134	134.5
Int_Med_cMyc_ring	3.73320465	6.11277104	7.48547539	5.777150358	82	6.18060072	188	135
Int_Med_RB_cyto	3.90328699	4.14491265	6.69540765	4.914535763	132	7.84278521	138	135
Int_MeanEdge_pH2AX_cell	3.72936611	3.21532543	4.34427007	3.762987199	223	12.2396941	49	136
Int_Med_cFos_cyto	3.18410385	5.39118323	8.05822104	5.544502705	94	6.55332045	179	136.5
Int_Med_DNA_cell	3.98348208	4.62474811	6.62261864	5.076949608	122	7.35575537	151	136.5
Int_MeanEdge_pAKT_cell	3.93582551	2.87535113	5.00649125	3.939222629	210	10.8143522	64	137
Int_Med_STAT3_cell	4.616702	6.93934985	7.49122487	6.349092238	61	5.35588276	216	138.5
Int_Med_pH2AX_ring	4.90080893	3.51602315	5.02058855	4.479140212	168	8.79308781	112	140
Int_Med_pp27_nuc	2.66744081	6.48142177	12.5356683	7.22817695	40	2.33928496	241	140.5
Int_Med_pRB_cell	4.92708714	2.55849995	4.71035089	4.06531266	198	9.83460327	86	142
Int_Med_BP1_ring	3.44199374	6.09305867	5.6025141	5.045855501	124	7.14201314	161	142.5
Int_Med_pSTAT3_ring	5.60199049	5.79418438	7.2966793	6.230951387	66	5.13064955	220	143
Int_Med_pERK_cyto	3.07394253	2.06541511	7.54977615	4.229711263	190	9.39469528	97	143.5
Int_Med_pp21_ring	5.42275889	3.61241668	2.33850328	3.791226281	218	10.4654632	69	143.5
Int_Med_pSTAT3_cyto	3.78891447	4.76368602	5.82558884	4.792729777	143	7.63551283	144	143.5
Int_Med_RSK1_cell	2.21297326	4.89100049	4.94992547	4.017966408	202	9.52033592	92	147
Int_Med_p21_ring	6.51355476	5.30859936	4.58610858	5.469420899	96	5.95934856	199	147.5
Int_Med_CDK6_cell	1.73158848	5.13838591	3.01039853	3.293457638	236	10.8323774	62	149
Int_MeanEdge_p16_cell	6.30801991	3.58416152	1.58837888	3.826853437	216	9.94566227	83	149.5
Int_Med_bCat_cyto	2.26463329	5.14531278	6.93608094	4.782009002	144	7.28064456	156	150
Int_Med_pp65_ring	4.4165511	5.07569751	3.75331578	4.415188131	177	8.46163947	124	150.5
Int_MeanEdge_pSTAT3_cell	4.49103014	7.38015797	1.76208136	4.544423156	163	7.79081269	139	151
Int_Med_YAP_cell	4.91257764	9.58074264	3.87690459	6.123408292	71	3.64674757	232	151.5
Int_Med_pGSK3b_ring	4.10643674	4.75103382	2.80015091	3.885873822	213	9.54269773	91	152
Int_Med_p27_cyto	2.87085859	4.54249601	5.09188822	4.168414273	195	8.9283455	110	152.5
Int_Med_Bcl2_cyto	3.75055525	3.66257174	5.90391472	4.439013903	175	8.08110635	131	153
Int_Med_pp21_cell	5.51400262	6.12621559	4.20673469	5.282317633	109	6.02051742	197	153
Int_Med_CDK6_ring	3.7773034	3.5985712	4.60186543	3.992580009	205	9.21701238	102	153.5
Int_Med_RB_ring	4.33181695	3.87560251	6.56828379	4.925234413	130	6.59047235	178	154
Int_Med_YAP_cyto	4.39053189	7.32316491	1.01043746	4.241378084	189	8.60470905	119	154
Int_Med_pp38_cyto	3.76720005	3.15192777	4.44927934	3.789469054	219	9.64953954	90	154.5
Int_Med_AKT_ring	4.5524407	4.56130293	6.51778729	5.210510307	113	5.88153634	200	156.5
Int_Med_pH2AX_cyto	6.09908874	4.09313634	4.65395947	4.948728185	128	6.30866381	185	156.5
Int_Med_pRSK_cyto	4.60294866	4.47098245	4.73656116	4.603497419	159	7.3177616	155	157
Int_Med_pS6_nuc	6.77382029	5.1607708	6.52032282	6.151637972	70	2.01111787	244	157
Int_Med_YAP_ring	2.60279722	6.61416095	2.9010191	4.039325756	200	8.73757606	115	157.5
Int_MeanEdge_BP1_cell	5.77738518	4.91209823	3.59114192	4.760208441	146	6.78727122	172	159
Int_Med_pSTAT3_cell	2.46926475	5.13172695	7.02598664	4.875659449	136	6.4534768	183	159.5
Int_Med_cFos_ring	3.61900117	3.65961777	7.2652452	4.847954713	139	6.49407723	181	160
Int_Med_p53_cyto	2.29093988	5.50567154	5.62515648	4.473922636	170	7.33415629	152	161
Int_MeanEdge_pp65_cell	6.77806372	2.46563092	3.89512166	4.379605436	179	7.62538914	145	162
Int_Med_Fra1_cyto	4.18252185	4.58647219	4.30109667	4.356696902	183	7.64031155	143	163
Int_Med_p27_cell	4.34207644	6.77931716	4.75785573	5.293083107	107	4.85775725	224	165.5
Int_Med_pp65_cyto	4.85785826	4.41959419	1.97106725	3.749506565	227	9.10407025	105	166

Int_Med_cycE_ring	2.94590065	5.50818609	4.874773	4.442953247	174	7.18931856	159	166.5
Int_MeanEdge_pRSK_cell	1.51122982	4.70584632	6.43956815	4.218881429	191	7.61541916	146	168.5
Int_Med_ERK_cyto	4.27839303	5.47283905	4.95842134	4.903217808	134	5.77580434	204	169
Int_Med_p53_cell	3.52461658	5.67501158	5.27023109	4.823286417	142	6.02534608	196	169
Int_Med_S6_cyto	4.61704261	5.63646229	4.93002351	5.061176138	123	5.36259887	215	169
Int_Med_STAT3_ring	3.98087905	6.81102343	5.06916274	5.28702174	108	3.9993453	230	169
Int_MeanEdge_cFos_cell	3.95434241	4.39862522	5.92333529	4.758767641	148	6.06242672	192	170
Int_Med_RSK1_nuc	4.8028748	4.21267976	5.19011896	4.735224506	149	6.0778274	191	170
Int_Med_pRB_ring	1.91282293	4.84798921	5.86098102	4.207264386	192	7.4152418	150	171
Int_MeanEdge_Bcl2_cell	3.48766111	4.51830564	6.60237095	4.869445902	137	5.75689416	206	171.5
Int_MeanEdge_PCNA_cell	3.48295308	5.40715846	4.24786118	4.379324238	180	7.00212376	164	172
Int_Med_S6_ring	5.63982994	2.07301669	4.32857564	4.013807423	203	7.65252697	142	172.5
Int_MeanEdge_CDK6_cell	3.95603496	5.16309492	6.72195647	5.280362118	110	2.37420033	240	175
Int_Med_cJun_cyto	4.03745544	4.38066431	7.14377041	5.187296719	116	2.53143767	239	177.5
Int_Med_cFos_cell	5.11343295	3.05647907	6.64399934	4.937970454	129	4.25995971	227	178
Int_Med_pAKT_cyto	2.82504452	1.94982454	3.7332236	2.836030887	243	8.7192243	116	179.5
Int_Med_CDK4_ring	3.0400309	3.05299911	4.92168651	3.671572177	229	8.06146162	132	180.5
Int_Med_DNA_cyto	1.89360996	4.68466063	5.4612225	4.013164363	204	7.20267686	157	180.5
Int_Med_pRSK_ring	5.62040087	2.52129739	5.29556955	4.479089267	169	6.04899866	195	182
Int_Med_STAT3_nuc	3.28397401	2.48822466	7.36675879	4.379652484	178	6.18971406	187	182.5
Int_Med_bCat_ring	4.42839057	3.45816105	5.66422332	4.516924979	164	5.84370968	202	183
Int_Med_Bcl2_ring	2.02443153	6.68792917	4.24807636	4.320145687	186	6.5228212	180	183
Int_Med_GSK3b_cyto	2.09401541	4.97378498	6.91614577	4.661315388	154	5.53289585	213	183.5
Int_Med_pp53_cell	5.12702685	4.34852525	4.35118511	4.608912406	158	5.59950902	211	184.5
Int_Med_pCHK1_cell	3.47963057	4.62530523	1.62092402	3.24195327	237	8.0306869	133	185
Int_Med_pGSK3b_cyto	2.10980797	3.48252026	6.10212556	3.898151261	212	7.20251475	158	185
Int_Med_p27_ring	3.78015364	6.90413955	2.80465774	4.496316978	167	5.76062401	205	186
Int_Med_cJun_ring	3.00806586	4.95579234	5.95809039	4.640649532	156	5.14460004	219	187.5
Int_Med_CDK4_cyto	1.99039834	5.78940954	4.10763449	3.96248079	207	6.89689812	170	188.5
Int_Med_RSK1_ring	3.00006289	6.36471443	3.95124837	4.43867523	176	5.84770459	201	188.5
Int_Med_ERK_ring	0.46677905	6.36460987	6.22703393	4.352807615	184	6.05943476	194	189
Int_Med_BP1_cyto	3.22674723	4.61508764	4.70080689	4.180880585	194	6.23056948	186	190
Int_Med_pp27_ring	4.78017545	4.47169094	4.90751152	4.71979264	150	3.29599001	233	191.5
Int_Med_cycE_cyto	0.78841858	4.60919656	6.09747935	3.831698162	215	6.87870512	171	193
Int_Med_p21_cell	4.16771125	3.23736004	3.92929609	3.778122458	221	7.00052255	165	193
Int_Med_cycE_cell	4.38090899	4.2809485	3.66606283	4.109306773	196	6.06040184	193	194.5
Int_MeanEdge_pp21_cell	2.61077954	2.9564137	7.95002271	4.505738649	165	4.21573133	228	196.5
Int_MeanEdge_S6_cell	1.22839258	5.011611	4.42302903	3.554344205	233	7.18313825	160	196.5
Int_MeanEdge_Cdh1_cell	3.75537898	5.48805634	2.01073465	3.751389986	226	6.73654449	173	199.5
Int_Med_AKT_cyto	3.00033197	3.65365714	6.3285156	4.32750157	185	5.34096127	217	201
Int_MeanEdge_pp53_cell	4.08965549	4.30739517	0.78267399	3.059908217	240	7.04486255	163	201.5
Int_Med_pp21_cyto	3.78456162	3.96288928	4.55135258	4.099601159	197	5.74936505	207	202
Int_Med_pp27_cyto	3.56170279	6.03056853	3.90445965	4.498910322	166	2.53272971	238	202
Int_Med_pRSK_nuc	3.43779458	0.1616543	4.62107189	2.740173589	246	6.96678298	166	206
Int_Med_STAT3_cyto	2.26117393	1.97647059	4.18859083	2.808745117	244	6.95371978	168	206
Int_Med_p21_cyto	4.60668904	3.47182753	4.52174508	4.200087216	193	4.88621577	223	208
Int_Med_pCHK1_ring	4.89981644	2.5546202	5.93878432	4.464406988	171	1.45071753	245	208
Int_MeanEdge_p21_cell	4.11136447	4.80480248	2.94641906	3.954195338	208	5.65804069	210	209
Int_Med_pCHK1_cyto	4.25520354	4.82839229	3.743584	4.275726611	187	3.89906174	231	209
Int_MeanEdge_STAT3_cell	3.74726016	3.06241517	3.99119208	3.600289137	232	6.15874721	189	210.5
Int_MeanEdge_RB_cell	5.09147813	1.91318283	4.35847029	3.787710415	220	5.81513477	203	211.5
Int_Med_pp65_cell	3.49684502	4.07947592	1.42693276	3.001084567	241	6.48154479	182	211.5
Int_Med_pRSK_cell	4.6105701	2.09166759	5.14502421	3.9490873	209	5.44857907	214	211.5
Int_MeanEdge_cycD1_cell	4.72239741	4.70370284	3.67847012	4.368190125	181	0	246	213.5
Int_MeanEdge_p27_cell	1.46452132	3.73235122	6.86783318	4.021568571	201	4.40719178	226	213.5
Int_MeanEdge_pRB_cell	2.51885149	5.39924597	2.94706337	3.621720274	230	6.00166281	198	214
Int_Med_pp53_cyto	4.34849715	1.1822428	6.26764086	3.9327936	211	4.61715105	225	218
Int_MeanEdge_p14ARF_cell	6.32282965	1.22446359	4.06126091	3.869518052	214	4.10484621	229	221.5
Int_MeanEdge_pCHK1_cell	4.9657079	4.42466899	1.43335061	3.607909163	231	5.24852314	218	224.5
Int_Med_Fra1_ring	5.69680252	2.2193392	0.71609187	2.877411196	242	5.7162633	208	225

Int_Med_p38_ring	2.76652923	3.83335658	4.48029895	3.693394918	228	4.9753727	222	225
Int_MeanEdge_RSK1_cell	4.28425377	0	5.22818698	3.170813582	239	5.56329996	212	225.5
Int_Med_pp27_cell	3.36066176	2.89968313	5.19793787	3.819427586	217	2.65365851	237	227
Int_Med_pp38_cell	4.14761307	2.55116917	1.6037117	2.76749798	245	5.6754151	209	227
Int_Med_pp38_ring	3.25109008	2.84711514	3.92057879	3.339594672	235	5.01441686	221	228
Int_Med_pH2AX_cell	4.80271321	2.51171513	3.95413932	3.756189222	224	3.22468787	234	229
AreaShape_FormFactor_cell	3.63719929	3.80963369	3.84224321	3.763025397	222	2.3336471	242	232
Int_Med_Bcl2_cell	3.62895536	2.73243616	4.90104999	3.754147172	225	2.23208761	243	234
Int_Med_RSK1_cyto	4.08804948	1.98846851	4.22209866	3.432872216	234	2.90749489	236	235
Int_Med_AKT_nuc	3.61833815	1.51638976	4.41451295	3.183080285	238	3.01528954	235	236.5